Low-Cost Rechargeable Battery Using Pencil Graphite as Ion Intercalation / De-Intercalation Electrode

by

Md. Jahidul Islam

A thesis submitted in partial fulfillment of the requirements for the degree of
Master of Science in Chemistry

Khulna University of Engineering & Technology

Khulna 9203, Bangladesh

June 2018

Declaration

This is to certify that the thesis work entitled "*Low-Cost Rechargeable Battery Using Pencil Graphite as Ion Intercalation / De-Intercalation Electrode*" has been carried out by *Md. Jahidul Islam* in the Department of Chemistry, Khulna University of Engineering and Technology, Khulna, Bangladesh. The above thesis work or any part of this work has not been submitted anywhere for the award of any degree or diploma.

_____
Signature of Supervisor

_____
Signature of Candidate

Certificate of Research

Approval

This is to certify that the thesis work submitted by Md. Jahidul Islam with title "**Low-Cost Rechargeable Battery using Pencil Graphite as Ion Intercalation / Deintercalation Electrode**" has been approved by the board of examiners for the partial fulfillment of the requirements for the Degree of Master of Science in the Department of Chemistry, Khulna University of Engineering & Technology, Khulna, Bangladesh in June, 2018.

BOARD OF EXAMINERS

1. _____
   Dr. A. B. M. Mamun Jamal   Chairman
   Assistant Professor
   Department of Chemistry   (Supervisor)
   Khulna University of Engineering & Technology
   Khulna-9203, Bangladesh

2. _____
   Head   Member
   Department of Chemistry
   Khulna University of Engineering & Technology
   Khulna-9203, Bangladesh

3. _____
   Dr. Mohammad Abu Yousuf   Member
   Professor, Department of Chemistry
   Khulna University of Engineering & Technology
   Khulna-9203, Bangladesh

4. _____
   Dr. Md. Mizanur Rahman Badal   Member
   Professor, Department of Chemistry
   Khulna University of Engineering & Technology
   Khulna-9203, Bangladesh

5. _____
   Dr. Md. Qamrul Ehsan   Member
   Professor, Department of Chemistry   (External)
   University of Dhaka
   Dhaka-1000, Bangladesh

Acknowledgement

Abstract

Remarkable improvement in utilizing renewable energy has pioneered to a critical demand for the large-scale energy storage system considering cost, safety and environmental aspect. Zn/Al-ion batteries are eco-friendly and advantageous over acid or alkali-based batteries as it is possible to utilize Zn metal as the negative electrode in aqueous medium. Here a Zn/Al-ion battery is developed using Pencil graphite, coated with graphene by cyclic voltammetry (CV), as the positive electrode and Zn metal as the negative electrode in an aqueous $AlCl_3/Zn(CH_3COO)_2$ (0.5/0.5M) electrolyte. The Zn/Al-ion cell shows average discharge voltage plateaus around 1.0 V which offers a specific cathode capacity of ~54.1 mAh g^{-1} at a constant current density of 55 mA g^{-1} and exhibits capacity retention of more than ~95.8% over 100 cycles without any formation of dendrite at the negative electrode (Zn). Reversible Al^{3+} or $[Al(H_2O)_6]^{3+}$ ion intercalation/de-intercalation storage process involving graphene coated pencil graphite (positive electrode) during charge-discharge cycling is proposed on the basis of CV, Electrochemical impedance spectroscopy (EIS), Scanning electron microscopy (SEM) and Energy dispersive X-ray spectroscopy (EDX) analysis.

Contents

LIST OF TABLES

LIST OF FIGURES

LIST OF ILLUSTRATIONS

LIST OF ABBREVIATIONS

Abbreviations	Extensions/ Elaborations
AC	Alternating Current
ARB	Aqueous Rechargeable Battery
ARSB	Aqueous Rechargeable Sodium Battery
ATR	Attenuated Total Reflectance
CE	Counter Electrode
CV	Cyclic Voltammetry
3DGF	Three Dimensional Graphitic Foam
DES	Deep Eutectic Solvents
DOD	Depth Of Discharge
EDX	Energy Dispersive X-Ray Spectroscopy
EIS	Electrochemical Impedance Spectroscopy
EMC	Ethyl Methyl Carbonate
EMIC	Ethyl Methyl Imidazolium Chloride
FTIR	Fourier Transform Infrared Spectroscopy
GFP	Glass Fiber Paper
GPGE	Graphene Coated Pencil Graphite Electrode
GO	Graphene Oxide
GOPGE	Graphene Oxide Coated Pencil Graphite Electrode
IHP	Inner Helmholtz Plane
ILA	Ionic Liquid Analog
LSV	Linear Sweep Voltammetry
OCP	Zero Current Potential/ Open Circuit Potential
OHP	Outer Helmholtz Plane
PGE	Pencil Graphite Electrode
SCE	Saturated Calomel Electrode
SDS	Sodium Dodecyl Sulfate
SEM	Scanning Electron Microscopy
RE	Reference Electrode
RTIL	Room Temperature Ionic Liquid
WE	Working Electrode

Nomenclature

A	Surface Area
a_i	Activity of Relevant Species
C	Bulk Concentration
C	Rated Capacity of the Battery in Ah
C_{nf}	Non-faradic Capacitance
C_s	Faradic Components of Impedance
D_o	Diffusion Coefficient of Oxidized Species
D_r	Diffusion Coefficient of Reduced Species.
D_s	The Diffusion Coefficient
E^o	Standard Electrode Potential
ΔE	Voltage Separation
F	Faraday's Constant
ΔG^o	Standard Free Energy
I	Charge Discharge Current
I_c	Capacity Current
I_f	Faradic Current
M	Multiple or Fraction Of Concentration
n	Mole Numbers
N	Time (In Hours) for Rated Capacity
O	Oxidized Species
Q	Constant Phase Element
R	Universal Gas Constant
R	Reduced Species
R_{cell}	Cell Resistance
R_{ct}	Charge Transfer Resistance
R_e	Electrolyte Resistance
R_s	Solution Resistance
t	Time
T	Absolute Temperature
v	Scan Rate (mV/s)
w	Warburg Impedance

CHAPTER I

Introduction

1.1 General

Alarming concerns of environmental pollution have triggered the search for alternative energy resources such as tidal, solar, wind, geothermal energy etc. This have dictated a emerging necessity of reliable energy storage systems for large-scale application [1]. The increasing interest in energy storage for the grid can be attributed to multiple factors, including the capital costs of managing peak demands, the investments needed for grid reliability, and the integration of renewable energy sources. Although existing energy storage is dominated by pumped hydroelectric, there is the recognition that rechargeable battery systems can offer a number of high-value opportunities, provided that lower costs can be obtained [2].
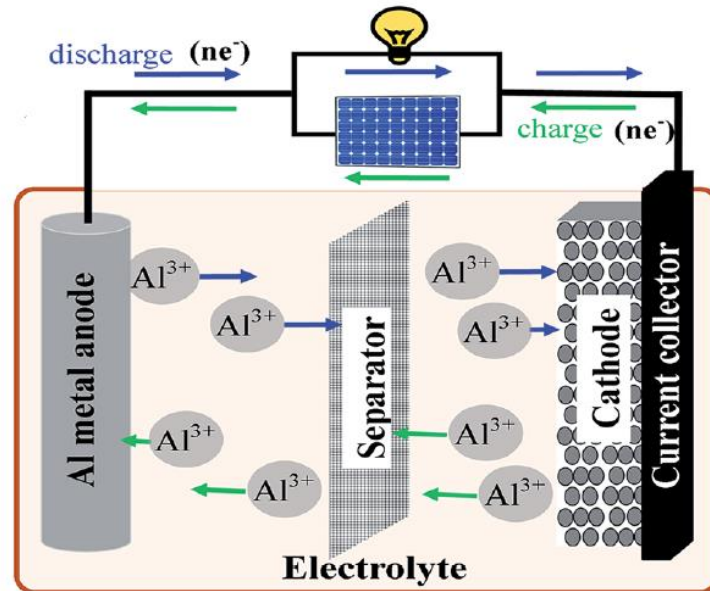
Scheme 1: Schematic representation of the redox reactions for aqueous rechargeable battery during the charge and discharge process.[3]

To getrid of the dependence on conventional fossil fuels, large-scale storage devices for renewable energy needs to be implemented which requires inexpensive, high-rate capable and long cycle life providing rechargeable battery technology.

1.2 Battery

A battery is a device that converts the chemical energy contained in its active materials directly into electric energy by means of an electrochemical oxidation-reduction (redox) reaction. In the case of a rechargeable system, the battery is recharged by a reversal of the process. This type of reaction involves the transfer of electrons from one material to another through an electric circuit.

While the term ''battery'' is often used, the basic electrochemical unit being referred to is the "Cell". A battery consists of one or more of these cells, electrically connected in an appropriate series or parallel arrangement, or both, depending on the desired output voltage and capacity (or current levels).

1.2.1 Battery Components

The cell consists of three major components:

i. The anode or negative electrode—the reducing or fuel electrode—which gives up electrons to the external circuit and itself is oxidized during the electrochemical reaction.

ii. The cathode or positive electrode—the oxidizing electrode—which accepts electrons from the external circuit and is reduced during the electrochemical reaction and the electrolyte ions are stored within the cathode when the cell is discharged.

iii. The electrolyte—the ionic conductor—which provides the medium for transfer of charge, as ions, inside the cell between the anode and cathode. The electrolyte is typically a liquid, such as water or other solvents, with dissolved salts, acids, or alkalis to impart ionic conductivity. Some batteries use semi-solid electrolytes, which are ionic conductors at the operating temperature of the cell.

1.3 Working Principle of Battery

In general, there are five components that constitute a cell. These components are two electrodes, electrolyte, and two current collectors. The main function of the electrodes is to be reduced or oxidized over a potential range measured in volts (V). The electrolyte serves as an ionic conductor between the electrodes and must be electronically insulating. The current collectors are an electrically conducting material, usually a metal that are directly in contact with each electrode. The current collectors are attached to each other by an external circuit. An Al-ion battery exhibits the electrochemical cell functions because of the potential difference between the two electrodes. It is energetically favorable for the two

electrodes to come towards an equilibrium potential that is lower than the initial open-circuit cell potential where they are stable. Equilibrium between the electrodes is achieved by the oxidation of one electrode and the reduction of the other electrode. The electrode that is reduced is called the cathode, while the electrode that is oxidized is called the anode. These reactions are accomplished by two distinct paths for ions and electrons. The electrons travel through the external circuit from the anode to the cathode. At the same time, the ions travel in the same direction as the electrons between the two electrodes through the electrolyte. This completes the redox reaction of the two electrodes, as showed clearly in Scheme 1.

Generally, the basic working principle of Al-ion batteries is based on aluminum ion (Al^{3+}) reversible de-intercalation and intercalation processes involving cathode materials. As a result, during charge/discharge, Al^{3+} ions flow between the anode and the cathode, enabling the conversion of chemical energy into electrical energy and the storage of electrochemical energy within the battery.

The electrolyte should be ionically conducting and electronically insulating, however the actual properties of the electrolyte is much more complicated. During the first cycle, a solid–electrolyte-interphase (SEI) layer will be formed on the surface of electrodes due to the decomposition of electrolyte. The typical electrochemical reactions involved in a typical AIB cell are described in Scheme 1.

The electrolyte and separator combination within a aluminum ion battery is a key component which requires some important considerations for optimal battery performance. The ionic conductivity of the electrolyte should be high to reduce internal cell resistance. In addition the stability of the electrolyte is an important factor in two ways;

i. a high chemical stability prevents decomposition of the electrolyte on highly reducing anodes or oxidizing cathodes and

ii. a large voltage window of electrochemical stability as determined by the voltage difference between the cathode and anode.

Furthermore a low melting point and a high boiling point can provide adequate conductivity and enhance the battery safety by preventing solidification of the electrolyte and explosive reactions at high temperatures. Non-toxicity of the electrolyte in terms of environmental concerns and ease of handling allow for the scale-up use of a suitable material, and lastly, an electrolyte at an affordable cost as compared to other power sources

will aid in its commercial viability [4]. The function of the separator is to prevent short circuit between the two electrodes and to provide abundant channels for transportation of electrolyte-ions during the process of charging/discharging.

1.4 Opportunities in Aluminum ion Batteries

Aluminum ion battery (AIB) is a type of rechargeable battery in which Al-ions move from the negative electrode to the positive electrode during discharge and back when charging. Aluminum ion electrodes are conventionally intercalation materials where the Al^{3+} ions reside in between the layers and spaces in the lattice structures of the host material. A material's tendency to accept Al^{3+} ions within its structure determines its storage capacity and viability as an electrode material.

Rechargeable aluminum ion batteries are of much interest in recent years due to some benefits over Li or Na ion based battery. Firstly, aluminum is of low cost owing to the third most abundant element in the Earth's crust. Then, an Al-ion based electrochemical system involves three-electron redox properties in charging/discharging reactions, which renders facile storage capability compared to monovalent (e.g. Na^+ or Li^+) ion based battery with one electron transportation.

Poly-thiophene and poly-pyrrole (conducting polymers) [5], VO_2 [6], V_2O_5 [7, 8], graphite on Ni-foam [9], fluorinated graphite [10] etc. have been revealed to be emerging for the Al-ion battery as electrode substances in an $AlCl_3$/ionic liquid electrolyte. For instance, the Al//graphitic foam based battery in an $AlCl_3$/EMIC (1-ethyl-3-methylimidazolium chloride) electrolyte showed a notable charge/discharge life up to 7500 cycles [9]. But, ionic liquid electrolyte (ILA) used is highly expensive and hygroscopic in nature which requires sophisticated assembly environment.

Hence, it is promising to shift from costly ionic liquid electrolyte to a low-priced water based electrolyte. Aqueous rechargeable batteries (ARBs) are essentially secure as they substitute flammable organic electrolyte solutions with aqueous ones. Besides, water based electrolytes are inexpensive, and fabrication practice of these batteries is simple as well. Furthermore, the conductivity of ions in aqueous medium (up to 1 S cm^{-1}) is higher than that of organic medium (~1−10 mS cm^{-1}), which favours high rate capability and high power density [11, 12] appropriate for rising applications [1]. For grid storage, factors such as expenses, rate capability and durability are more significant than heaviness and energy

density. Moreover, for frequency regulation rapid response equivalent systems are particularly important for grid storage [13].

Currently, many kinds of ARBs have been widely invented, such as KCuFe-(CN)$_6$//PPy at activated carbon battery [14], FeO$_x$//Ni(OH)$_2$ battery [15], battery using Zn$_{0.25}$V$_2$O$_5$.nH$_2$O cathode [16], aqueous Zn ion battery [17, 18], Zn//Ni(OH)$_2$ or NiO battery [19, 20], aqueous rechargeable sodium battery (ARSB) [21-23], and aqueous rechargeable lithium ion battery (ARLB) [24-34].

1.5 Anode

In a secondary cell, anode is the negative pole that is oxidized during the battery discharge reaction but the positive pole during charge where the electrolyte ions are stored when the cell is fully charged.

The basic requirements for an anode material are that the material should have minimal volume expansion and resulting stress during charge/discharge process, high electronic conductivity, low irreversible capacity during initial charging or intercalation process, stable under wide operating temperature window in a highly reducing environment, and low specific surface area (typically $<$2 m^2/g) for optimal performance and safety [35].

1.5.1 Motivation for Metallic Zn as Anode Material

In case of anode materials for ARBs, exploring attempt has expanded Na$^+$ and K$^+$ systems [36-39], Li$^+$ intercalation substances [40-42], and also the intercalation chemistry of multivalent cations that engage in multiple electron transfer [43-46]. Among them, Zn anode based batteries (containing aqueous electrolyte of Zn^{2+} coupled with Al^{3+} ions) are useful due to the following properties of Zn metal, that include: good abundance and large-scale manufacture, thus making it low cost [47]; low reduction potential (-0.76V versus standard hydrogen electrode) compared to other materials used as negative electrode in aqueous system [47]; low toxicity [50]; and stability in water owing to a high overpotential for H$_2$ gas evolution [50]. This stability provides a large potential window (~2V) for zinc-ion battery in aqueous medium applying a metallic Zn negative electrode (`anode'). Nanoporous `hyperdendritic' zinc foam offers additional promise [48]. Recently, an aqueous rechargeable zinc/aluminum ion battery has been reported where Zn metal is used as anode coupled with exfoliated graphitic cathode [49].

1.6 Cathode

The cathode is the positive electrode that is reduced during the spontaneous reaction. Transition metal oxides, pyrolytic graphites etc. have traditionally been the material of choice for cathodes used as aluminum ion battery components [5-10]. However, there is still focused interest to identify and develop anode and cathode materials that are more suitable in energy storing, while improving rate capability and safety.

This structural stability is a particular challenge during charging when most (ideally all) of the ions are removed from the cathode. During discharge Aluminum ions are inserted into the cathode material and electrons from the anode reduce the transition metal ions in the cathode to a lower valence.The key requirements for a successful cathode material in a rechargeable AIB are as follows:

i.   The material contains favorable interface formed at contact with electrolyte ions;

ii. Interacts with electrolyte ion in a very rapid reversible redox manner for both insertion and extraction processe;

iii. Reacts with Aluminum with a high free energy of reaction and electrode potential should vary little with Al^{3+} content;

iv. Good electronic conductor and demonstrate fast diffusion of electrons and Al^{3+};

v.   Stable within operating voltage range for charging and discharging;

vi. Less expensive, ease of synthesis and reproducibility and environmentally friendly.

The potential improvement of battery performance lies in several areas of battery development, with active materials and electrolyte chemistries being two with the biggest opportunities for growth. Because each of these fields is enormous in their breadth, a detailed and thorough investigation of any one specific area necessitates limiting the scope of study.

The cathode materials are commonly conducting materials or metal oxides with a layered structure which include insertion deinserttion type materials (e.g. graphite [9], fluorinated graphite [10], TiO_2 [50] etc.), conducting polymer-type materials (Poly-thiophene and poly-pyrrole [5]), and conversion-type materials (such as VO_2 [6], V_2O_5 [7, 8] etc.). At present, aqueous rechargeable aluminum ion batteries demonstrate prussian blue analogues

[51, 52] and TiO_2 [50] nanotubes to have the ability to intercalate Al-ion reversibly in aqueous electrolytes.

Graphite materials tend to be efficient intercalation materials, and the mechanism of storage that results in the stoichiometry of aluminum. Additionally, carbon anodes have been an excellent initial choice because of their high storage capacity, low cost, long cycle life, small volume change of < 9% upon ion intercalation, and negative reduction-oxidation potential versus the cathode. Ongoing investigations into overcoming this problem have lead to a variety of alternative cathode materials for aluminum ion battery.

1.6.1 Graphene-based Cathode

Graphene was discovered in 2004 which consists of a 2-D single layer planar nanosheet [53, 54] consisting of two equivalent sub-lattices of sp^2-hybridized carbon atoms connected by σ bonds [55]. Graphene has attracted much attention owing to remarkable properties such as good electrical conductivity [56, 57], large theoretical specific surface area (2630 m^2g^{-1}) [58, 59], thermal conductivity [60] and high Young's modulus (-1.0 TPa) [61, 62]. Graphene has revealed a new perception on carbon-based materials [63], as applications of graphene in anti-corrosion materials [64] sensors [65], optoelectronics [66], bio-electrochemistry [67] and energy storage systems [68-70], have been rapidly increasing and its bulk scale preparation at low cost by different processes has drawn much attention.
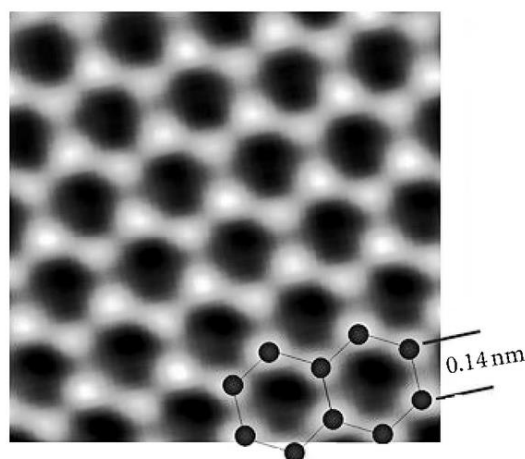
Figure 1.01: TEM image of 2-D honeycomb structure of carbon atoms in graphene.

Graphene-based electrodes have used as the positive electrodes in the vanadium redox batteries (VRBs), and they showed a better electrochemical performance than that of glassy carbon electrodes [71, 72].

1.6.2 Synthesis of Graphene

Electrochemical exfoliation can be applied for the production of graphene by either reduction of graphene oxide on the electrode surface or by direct treatment of a graphite as working electrode at ambient temperature and pressure [73-76]. Reducing graphene oxide into graphene using linear-sweep voltammetry (LSV) has been reported by method Zhou *et al.* [77]. Kakaei *et al.* studied graphene oxide powder exfoliation of at constant voltage in ionic liquids or surfactant solutions which is expensive and requires high voltage ($\geq$ $\pm 5V$) [78-80]. Exfoliation process to produce graphene from graphite powder is also done using cyclic voltammetry (CV) in sodium dodecyl sulfate (SDS) solution [81]. The electrochemical reduction of graphite powder in SDS solution on carbon paper has done by Kakaei and Gharibi [82]. Electrochemically cathodic exfoliation in ionic liquids has also been reported for production of graphene [83]. Gürsu *et al.* reported the formation of graphene can be achieved on the surface of a pencil graphite electrode as the working electrode in nitric acid solution by CV without any secondary step for electrode preparation and exfoliation process [84].

1.7 Spectroscopic Techniques for Material Characterization

1.7.1 Fourier Transformation Infrared Spectroscopy (FTIR)

FTIR is a technique used to obtain an infrared spectrum of absorption or emission of a solid, liquid or gas. An FTIR spectrometer simultaneously collects high spectral resolution data over a wide spectral range. This confers a significant advantage over a dispersive spectrometer, measuring intensity over a narrow range of wavelengths at a time.
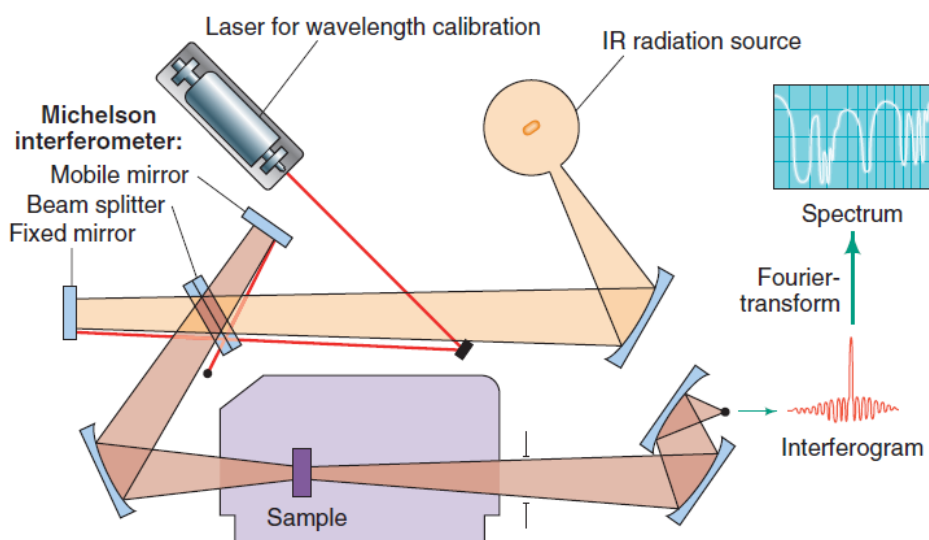
Scheme 2: A diagram of Fourier transform infrared (FTIR) spectrometer.

The term *Fourier-transform infrared spectroscopy* originates from the fact that a Fourier transform (a mathematical process) is required to convert the raw data into the actual spectrum. The interferogram in practice consists of a set of intensities measured for discrete values of retardation. The difference between successive retardation values is constant. Thus, a discrete Fourier transform is needed. An infrared spectrometer (Scheme 2) operates by passing a beam of IR radiation through a sample and comparing the radiation transmitted through sample with that transmitted in the absence of sample. Any frequencies absorbed by the sample will be apparent by the difference. The spectrometer plots the results as a graph showing absorbance versus frequency or wavelength.

1.7.1.1 Attenuated Total Reflectance (ATR)

ATR is one accessory of FTIR spectrophotometer to measure surface properties of solid or thin film samples rather than their bulk properties. Generally, ATR has a penetration depth of around 1 or 2 micrometers depending on your sample conditions.

1.7.2 Energy Dispersive X-ray Spectroscopy (EDX)

EDX is an analytical technique used for the elemental analysis or chemical characterization of a sample. It relies on an interaction of some source of X-ray excitation and a sample. Its characterization capabilities are due in large part to the fundamental principle that each element has a unique atomic structure allowing a unique set of peaks on its electromagnetic emission spectrum. [85]
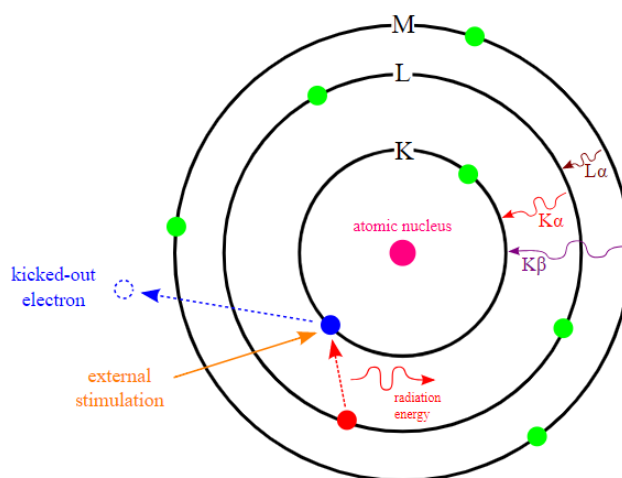
Figure 1.02: Working principle of Energy Dispersive X-ray spectroscopy.

To stimulate the emission of characteristic X-rays from a specimen, a high-energy beam of charged particles such as electrons or a beam of X-rays, is focused into the sample being

studied. At rest, an atom within the sample contains ground state electrons in discrete energy levels or electron shells bound to the nucleus. The incident beam may excite an electron in an inner shell, ejecting it from the shell while creating an electron hole where the electron was. An electron from an outer, higher-energy shell then fills the hole, and the difference in energy between the higher-energy shell and the lower energy shell may be released in the form of an X-ray. The number and energy of the X-rays emitted from a specimen can be measured by an energy-dispersive spectrometer. As the energies of the X-rays are characteristic of the difference in energy between the two shells and of the atomic structure of the emitting element, EDS allows the elemental composition of the specimen to be measured.[85]

1.7.3 Scanning Electron Microscopy (SEM)

SEM is a type of electron microscope that produces images of a sample by scanning the surface with a focused beam of electrons. The electrons interact with atoms in the sample, producing various signals that contain information about the surface topography and composition of the sample. The electron beam is scanned in a raster scan pattern, and the position of the beam is combined with the detected signal to produce an image. SEM can achieve resolution better than 1 nanometer. [86]
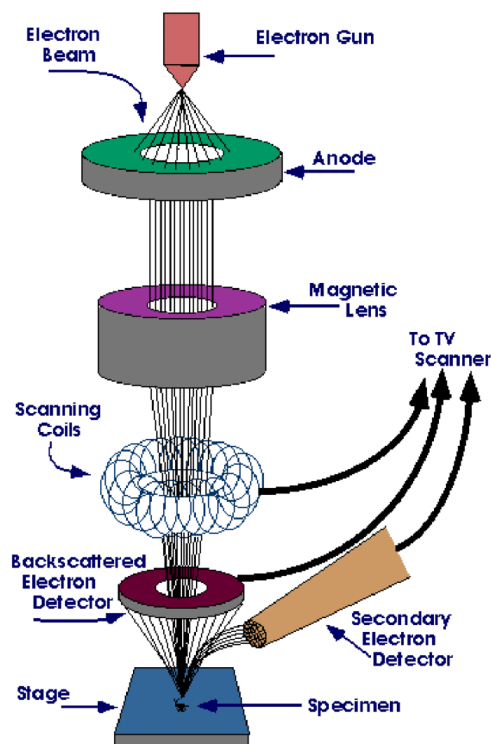
Scheme 3: Schematic diagram of Scanning electron microscope.

Specimens are observed in high vacuum in conventional SEM, or in low vacuum or wet conditions in variable pressure or environmental SEM and at a wide range of cryogenic or elevated temperatures with specialized instruments.

The most common SEM mode is the detection of secondary electrons emitted by atoms excited by the electron beam. The number of secondary electrons that can be detected depends, among other things, on specimen topography. By scanning the sample and collecting the secondary electrons that are emitted using a special detector, an image displaying the topography of the surface is created.

The signals used by a scanning electron microscope to produce an image result from interactions of the electron beam with atoms at various depths within the sample. Various types of signals are produced including secondary electrons (SE), reflected or back-scattered electrons (BSE) etc. Secondary electron detectors are standard equipment in all SEM.

In secondary electron imaging (SEI), the secondary electrons are emitted from very close to the specimen surface. Consequently, SEI can produce very high-resolution images of a sample surface, revealing details less than 1 nm in size. BSE are beam electrons that are reflected from the sample by elastic scattering. They emerge from deeper locations within the specimen and, consequently, the resolution of BSE images is less than SE images. However, BSE are often used in analytical SEM, along with the spectra made from the characteristic X-rays, because the intensity of the BSE signal is strongly related to the atomic number (Z) of the specimen. BSE images can provide information about the distribution, but not the identity, of different elements in the sample. Characteristic X-rays are emitted when the electron beam removes an inner shell electron from the sample, causing a higher-energy electron to fill the shell and release energy. The energy or wavelength of these characteristic X-rays can be measured by Energy-dispersive X-ray spectroscopy and used to identify and measure the abundance of elements in the sample and map their distribution.

Due to the very narrow electron beam, SEM micrographs have a large depth of field yielding a characteristic three-dimensional appearance useful for understanding the surface structure of a sample. A wide range of magnifications is possible, from about 10 times (about equivalent to that of a powerful hand-lens) to more than 500,000 times, about 250 times the magnification limit of the best light microscopes.[86]

1.8 Electrochemical Techniques for Battery/Cell Characterization

Many steady-state and impulse electroanalytical techniques are available to determine electrochemical parameters and assist in both improving existing battery systems and evaluating couples as candidates for new batteries.

1.8.1 Battery Discharging

The operation of a cell during discharge is also shown schematically in Figure 1.03 (a). When the cell is connected to an external load, electrons flow from the anode, which is oxidized, through the external load to the cathode, where the electrons are accepted and the cathode material is reduced [87]. The electric circuit is completed in the electrolyte by the flow of anions (negative ions) and cations (positive ions) to the anode and cathode, respectively.

The discharge reaction can be written, assuming a metal as the anode material and a cathode material such as chlorine (Cl_2), as follows:

Negative electrode: anodic reaction (oxidation, loss of electrons)

$$Zn \longrightarrow Zn^{2+} + 2e^-$$

Positive electrode: cathodic reaction (reduction, gain of electrons)

$$Cl_2 + 2e^- \longrightarrow 2Cl^-$$

Overall reaction (*discharge*)*:*

$$Zn + Cl_2 \longrightarrow Zn^{2+} + 2Cl^- \ (ZnCl_2)$$
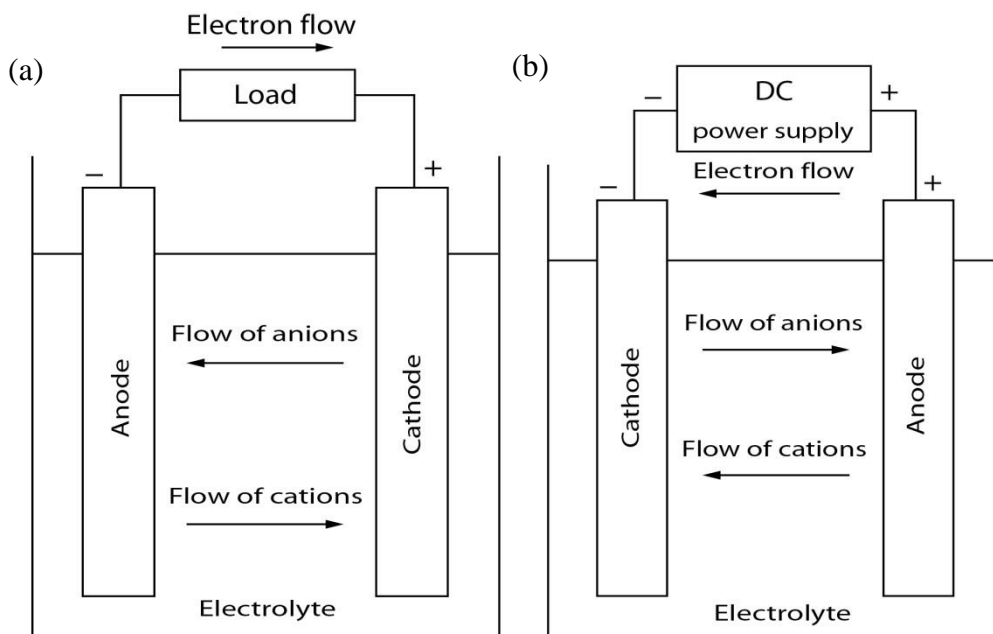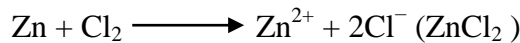
Figure 1.03: (a) Discharging and (b) Charging process of an electrochemical cell.[87]

1.8.2 Battery Charging

During the recharge of a rechargeable or storage cell, the current flow is reversed and oxidation takes place at the positive electrode and reduction at the negative electrode, as shown in Figure 1.03 (b). As the anode is, by definition, the electrode at which oxidation occurs and the cathode the one where reduction takes place, the positive electrode is now the anode and the negative the cathode. In the example of the Zn/Cl_2 cell, the reaction on charge can be written as follows:

Negative electrode: cathodic reaction (reduction, gain of electrons)

$$Zn^{2+} + 2e^- \longrightarrow Zn$$

Positive electrode: anodic reaction (oxidation, loss of electrons)

$$2Cl^- \longrightarrow Cl_2 + 2e^-$$
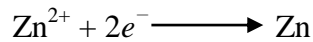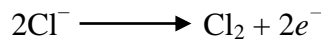
Overall reaction (*charge*): $Zn^{2+} + 2Cl^- \longrightarrow Zn + Cl_2$

1.8.3 Theoretical Voltage

The standard potential of the cell is determined by the type of active materials contained in the cell. It can be calculated from free-energy data or obtained experimentally. The standard potential of a cell can be calculated from the standard electrode potentials as follows (the oxidation potential is the negative value of the reduction potential):

Standard cell potential = Anode (oxidation potential) + cathode (reduction potential).

For example, in the reaction $Zn + Cl_2 \longrightarrow ZnCl_2$, the standard cell potential is:

$$Zn \longrightarrow Zn^{2+} + 2\,e^- \qquad E^{\circ}_{Zn/Zn^{2+}} = +0.76\ V \text{ (oxidation)}$$

$$Cl_2 \longrightarrow 2Cl^- - 2\,e^- \qquad E^{\circ}_{Cl2/Cl^-} = +1.36\ V \text{ (reduction)}$$

$$Zn + Cl_2 \longrightarrow Zn^{2+} + 2Cl^-\ (ZnCl) \qquad E^{\circ}_{cell} = +2.12\ V$$
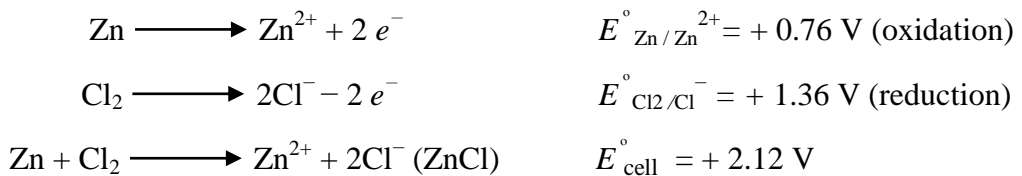
The cell voltage is also dependent on other factors, including concentration and temperature, as expressed by the Nernst equation.

In a cell, reactions essentially take place at two areas or sites in the device. These reaction sites are the electrode interfaces. In generalized terms, the reaction at one electrode (reduction in forward direction) can be represented by

$$aA + ne^- \rightleftharpoons cC$$
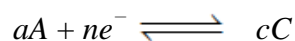
where *a* molecules of *A* take up *n* electrons *e* to form *c* molecules of *C*. At the other electrode, the reaction (oxidation in forward direction) can be represented by

$$bB + ne^- \rightleftharpoons dD$$
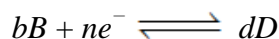
The overall reaction in the cell is given by addition of these two half-cell reactions

$$aA + bB \rightleftharpoons cC + dD$$

The change in the standard free energy ΔG° of this reaction is expressed as

$$\Delta G^{\circ} = -n\,FE^{\circ}$$

where F = Faraday constant (96,487 coulombs and E° = standard electromotive force

When conditions are other than in the standard state, the voltage E of a cell is given by the Nernst equation,

$$E = E^0 - \frac{RT}{nF} \ln \frac{a_C^c a_D^d}{a_A^a a_B^b}$$

Where, a_i = activity of relevant species

R = gas constant and

T = absolute temperature

The change in the standard free energy ΔG° of a cell reaction is the driving force which enables a battery to deliver electrical energy to an external circuit. The measurement of the electromotive force, incidentally, also makes available data on changes in free energy, entropies and enthalpies together with activity coefficients, equilibrium constants, and solubility products.

Direct measurement of single (absolute) electrode potentials is considered practically impossible.[88] To establish a scale of half-cell or standard potentials, a reference potential ''zero'' must be established against which single electrode potentials can be measured. By convention, the standard potential of the H_2/H^+ (aq) reaction is taken as zero and all standard potentials are referred to this potential.

1.8.3.1 Voltage Level

Different references are made to the voltage of a cell or battery:

i. The *theoretical voltage* is a function of the anode and cathode materials, the composition of the electrolyte and the temperature (usually stated at 25 °C).

ii. The *open-circuit voltage* is the voltage under a no-load condition and is usually a close approximation of the theoretical voltage.

iii. The *nominal voltage* is one that is generally accepted as typical of the operating voltage of the battery as, for example, 1.5 V for a zinc-manganese dioxide battery.

iv. The *closed-circuit voltage* is the voltage under a load condition.

v. The *working voltage* is more representative of the actual operating voltage of the battery under load and will be lower than the open-circuit voltage.

vi.   The *average voltage* is the voltage averaged during the discharge.

vii.   The *midpoint voltage* is the central voltage during the discharge of the cell/battery.

viii.   The *end* or *cut-off voltage* is designated as the end of the discharge. Usually it is the voltage above which most of the capacity of the cell or battery has been delivered. The end voltage may also be dependent on the application requirements.
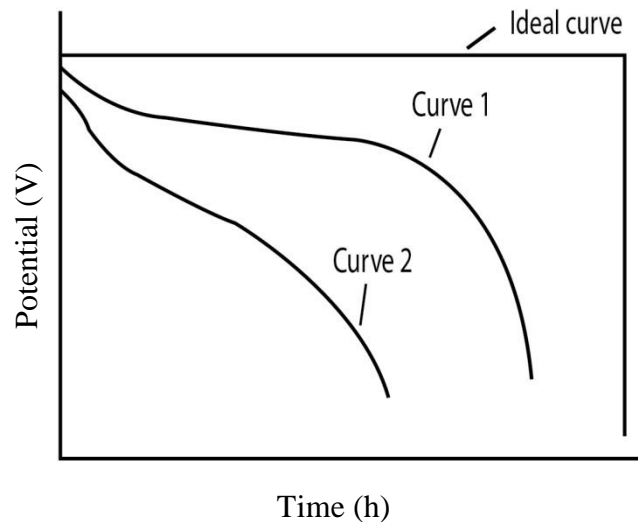
Figure 1.04: Characteristic curves of a battery cell under constant current discharging.[87]

When a cell or battery is discharged its voltage is lower than the theoretical voltage. The difference is caused by *IR* losses due to cell (and battery) resistance and polarization of the active materials during discharge. This is illustrated in Figure 1.04. In the idealized case, the discharge of the battery proceeds at the theoretical voltage until the active materials are consumed and the capacity is fully utilized. The voltage then drops to zero. Under actual conditions, the discharge curve is similar to the other curves in Figure 1.04. The initial voltage of the cell under a discharge load is lower than the theoretical value due to the internal cell resistance and the resultant *IR* drop as well as polarization effects at both electrodes. The voltage also drops during discharge as the cell resistance increases due to the accumulation of discharge products, activation and concentration, polarization, and related factors. Curve 2 is similar to curve 1, but represents a cell with a higher internal resistance or a higher discharge rate, or both, compared to the cell represented by curve 1. As the cell resistance or the discharge current is increased, the discharge voltage decreases and the discharge shows a more sloping profile.

The specific energy that is delivered by a battery in practice is; therefore, lower than the theoretical specific energy of its active materials, due to:

i. The average voltage during the discharge is lower than the theoretical voltage.

ii. The battery is not discharged to zero volts and all of the available ampere-hour capacity is not utilized as specific energy, (Watt hours/gram) = Voltage x Ampere hours/gram. The delivered specific energy is lower than the theoretical energy as both of the components of the equation are lower.
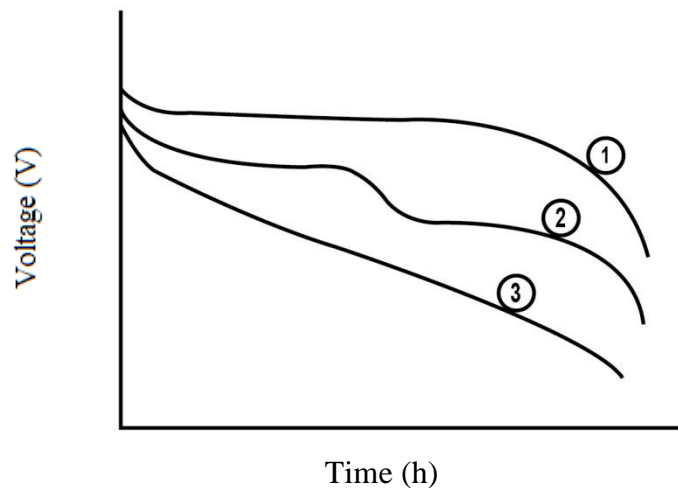
Figure 1.05: Characteristic discharge voltage profiles for various electrochemical systems.[87]

The shape of the discharge curve can vary depending on the electrochemical system, constructional features, and other discharge conditions. Typical discharge curves are shown in Figure 1.05. The flat discharge (curve 1) is representative of a discharge where the effect of change in reactants and reaction products is minimal until the active materials are nearly exhausted. The plateau profile (curve 2) is representative of two-step discharge indicating a change in the reaction mechanism and potential of the active materials. The sloping discharge (curve 3) is typical when the composition of the active materials, reactants, internal resistance, and so on, changes during the discharge, affecting the shape of the discharge curve similarly.

1.8.4 Theoretical Energy

The capacity of a cell can also considered on an energy (watt hour) basis by taking both the voltage and the quantity of electricity into consideration. This theoretical energy value is the maximum value that can be delivered by a specific electrochemical system:

$$\text{Watt hour (Wh)} = \text{voltage (V) x ampere-hour (Ah)}$$

In the Zn/Cl_2 cell example, if the standard potential is taken as 2.12 V, the theoretical Watt hour capacity per gram of active material (theoretical specific energy or theoretical

gravimetric energy density) is:

Specific Energy (Watt hours/gram) = 2.12 V x 0.394 Ah/g = 0.835 Wh/g or 835 Wh/kg

The average charge storage capacity and capacitance at the electrode surface was calculated using the following relations as reported earlier:

Specific capacity (mAh g^{-1}) of electrode material in a three electrodes system,

$$C = \frac{I \times t}{3.6 \times m}$$

where, I is the charge-discharge current (mA), t is the discharge time (s), m is the mass loading of active material (mg).

Specific capacitance (F g^{-1}) of electrode material in a three electrodes system

$$C = \frac{I \times t}{m \times V}$$

where, I is the charge-discharge current (mA), t is the discharge time (s), m is the mass loading of active material (mg) and V is the active potential regime (V).

1.8.5 Specific Energy and Energy Density of Practical Batteries

The maximum energy that can be delivered by an electrochemical system is based on the types of active materials that are used (this determines the voltage) and on the amount of the active materials that are used (this determines ampere-hour capacity). In practice, only a fraction of the theoretical energy of the battery is realized. This is due to the need for electrolyte and nonreactive components (containers, separators, electrodes) that add to the weight and volume of the battery. Another contributing factor is that the battery does not discharge at the theoretical voltage (thus lowering the average voltage), nor is it discharged completely to zero volts (thus reducing delivered ampere hours). Further, the active materials in a practical battery are usually not stoichiometrically balanced. This reduces the specific energy because an excess amount of one of the active materials is used.

1.8.6 Current Drain for Discharging

As the current drain of the battery is increased, the *IR* losses and polarization effects increase the discharge is at a lower voltage, and the service life of the battery is reduced. Figure 1.04 shows typical discharge curves as the current drain is changed. At extremely low current drains (curve 2) the discharge can approach the theoretical voltage and theoretical capacity.

"C" Rate. A common method for indicating the discharge, as well as the charge current of a battery, is the *C* rate, expressed as, $I = M \times C_n$

Where, I = discharge current *(A)*

C = numerical value of rated capacity of the battery, in ampere-hours *(Ah)*

n = time (in hours) for which rated capacity is declared

M = multiple or fraction of *C*

1.8.7 Cyclic Voltammetry (CV)

Essentially the technique applies a linearly changing voltage (ramp voltage) to an electrode. The principles behind cyclic voltammetry can be described with the reversible reduction of an oxidized species *O*,

$$O + ne^- \rightleftharpoons R \qquad \qquad ... (a)$$

In cyclic voltammetry, the initial potential sweep is represented by

$$E = E_i - v\,t \qquad \qquad ... (b)$$

where E_i = initial potential, t = time, v = rate of potential change or sweep rate ($\Delta V/s$)

The reverse sweep of the cycle is defined by

$$E = E_i + v't \qquad \qquad ... (c)$$

where v' is often the same value as v.

The effect of the electrical double layer on electrode kinetics that there is a capacitance effect at an electrode-electrolyte interface. Consequently the "true" electrode potential is modified by the capacitance effect as it is also by the ohmic resistance of the solution. Equation *(b)* should really be written in a form which described these two components. Equation *(d)* shows such a modification,

$$E = E_i - v\,t + r\,(\,i_f + i_c\,) \qquad \qquad ... (d)$$

where r = cell resistance, i_f = faradic current and i_c = capacity current

At small values of voltage sweep rate, typically below 1 mV/ s, the capacity effects are small and in most cases can be ignored. CV provides both qualitative and quantitative information on electrode processes. A reversible, diffusion-controlled reaction such as presented by equation *(a)* exhibits an approximately symmetrical pair of current peaks, as shown in Figure 1.06(a). The voltage separation ΔE of these peaks is

$$\Delta E = \frac{2.3\,RT}{nF} \qquad \qquad ... (e)$$

and the value is independent of the voltage sweep rate. In the case of the electrodeposition of an insoluble film, which can be, subsequently, reversibly reoxidized and which is not

governed by diffusion to and from the electrode surface, the value of ΔE is considerably less than that given by equation *(e)*, as shown in Figure 1.06 *(b)*.
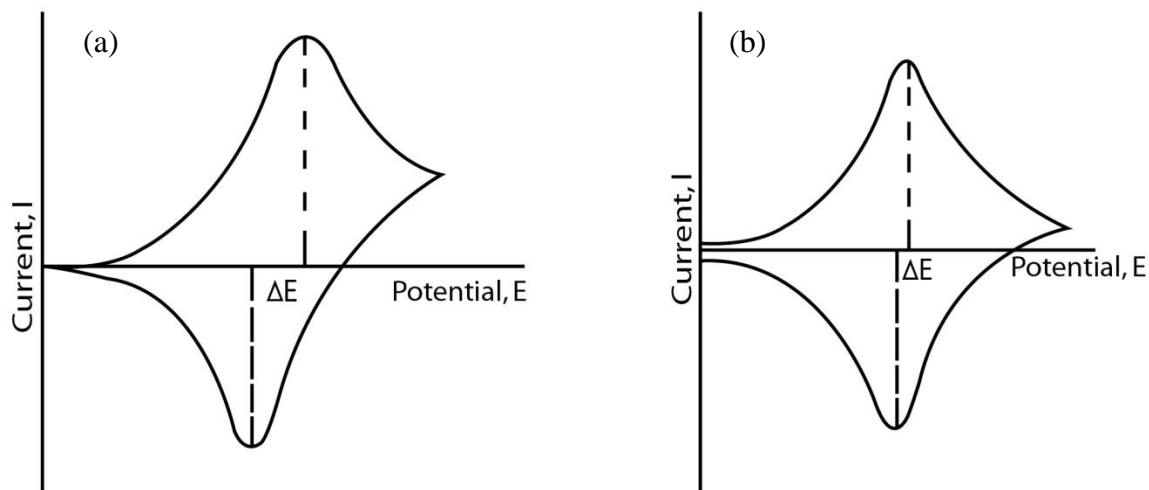
Figure 1.06: (a) CV of a reversible diffusion-controlled process,[87]

(b) CV of electroreduction and reoxidation of a deposited film.[87]

In the ideal case, the value of ΔE for this system is close to zero where for quasi-reversible processes, the current peaks are more separated, and the shape of the peak is less sharp at its summit and is generally more rounded, as shown in Figure 1.07.
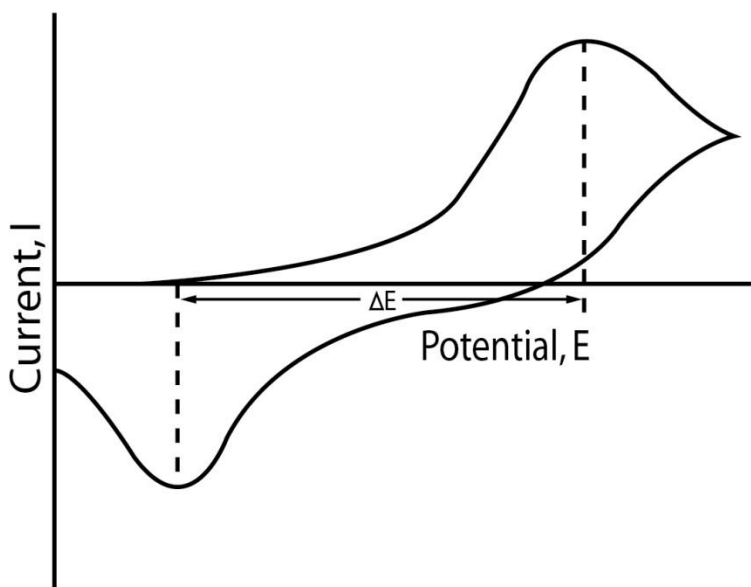
Figure 1.07: Cyclic Voltammogram of a quasireversible process.[87]

The voltage of the current peak is dependent on the voltage sweep rate, and the voltage separation is much greater than that given by equation *(d)*.

A completely irreversible electrode process produces a single peak, as shown in Figure 1.08. The peak potential is sweep-rate dependent, and, in the case of an irreversible charge transfer process for which the back reaction is negligible, the rate constant and transfer coefficient can be determined.
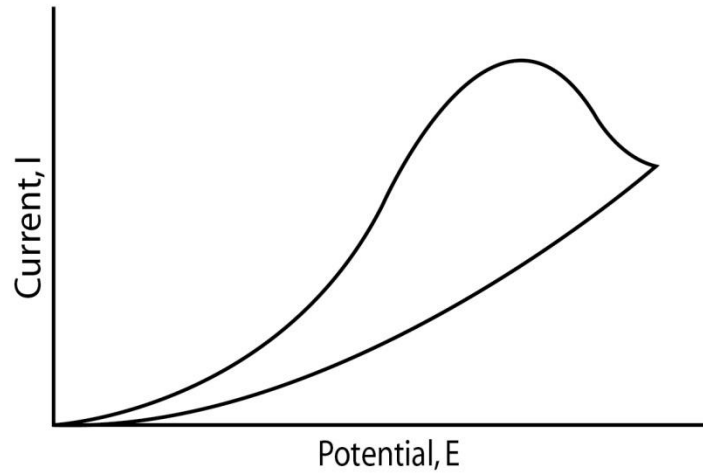
Figure 1.08: Cyclic voltammogram of an irreversible process.[87]

1.8.8 Chronopotentiometry

Chronopotentiometry involves the study of voltage transients at an electrode upon which is imposed a constant current. It is sometimes alternately known as galvanostatic voltammetry. In this technique, a constant current is applied to an electrode and its voltage response indicates the changes in electrode processes occurring at its interface. Consider, for example, the reduction of a species *O* as expressed by equation *(a)*.

Figure 1.09: Concentration profiles extending into bulk solution during constant-current depletion of species at electrode surface, $t_6 > t_0$ [87]

As the constant current is passed through the system, the concentration of *Oxidant (O)* in the vicinity of the electrode surface begins to decrease. As a result of this depletion, *O* diffuses from the bulk solution into the depleted layer, and a concentration gradient grows out from the electrode surface into the solution. As the electrode process continues, the concentration profile extends further into the bulk solution as shown in Figure 1.09. When the surface concentration of *O* falls to zero (at time t_6 in Figure 1.09), the electrode process can no longer be supported by electroreduction of *O*.
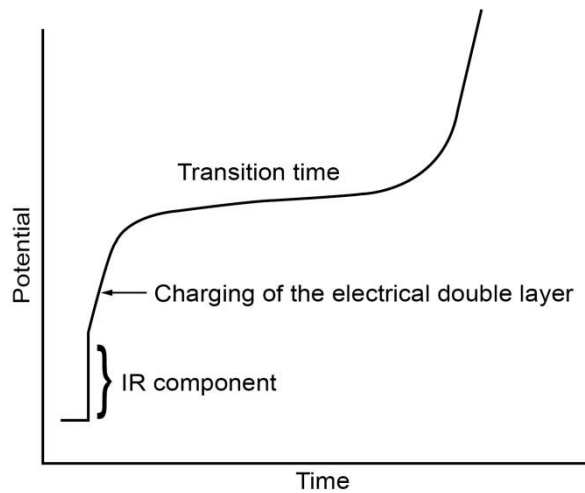
Figure 1.10: Chronopotentiogram of a system with significant resistance.[87]

An advantage of the technique is that it can be used conveniently to evaluate systems with high resistance. The trace conveniently displays segments due to the *IR* component, the charging of the double layer, and the onset of the faradaic process. Figure 1.10 shows these different features of the chronopotentiogram of solutions with significant resistance. If the solution is also one which does not contain an excess of supporting electrolyte to suppress the migration current, it is possible to describe the transition time of an electroreduction process in terms of the transport number of the electroactive species [89]

$$\sqrt{\tau} = \frac{\sqrt{\pi} \, n \, FC_o\sqrt{D}s}{2i(1-t_o)}$$

where D_S is the diffusion coefficient of the salt (not the ion) and t_o the transport number of the electroactive species. τ is the transition time, the period of time between the commencement of electoreduction and the sudden change in potential. This expression can be useful in battery research since many battery systems do not have supporting electrolyte.

For electroreduction of a species in the presence of excess supporting electrolyte is related into the diffusion coefficient of the electroactive species,

$$\sqrt{\tau} = \frac{\sqrt{\pi}\, n\, FC_{\mathrm{o}}\sqrt{D}}{2i}$$

where D is the diffusion coefficient of species O and the other symbols have their usual meanings.

1.8.3 Electrochemical Impedance Spectroscopy (EIS)

A more direct technique for studying electrode processes is to measure the change in the electrical impedance of an electrode by electrochemical impedance spectroscopy (EIS). To relate the impedance of the electrode-electrolyte interface to electrochemical parameters, it is necessary to establish an equivalent circuit to represent the dynamic characteristics of the interface.
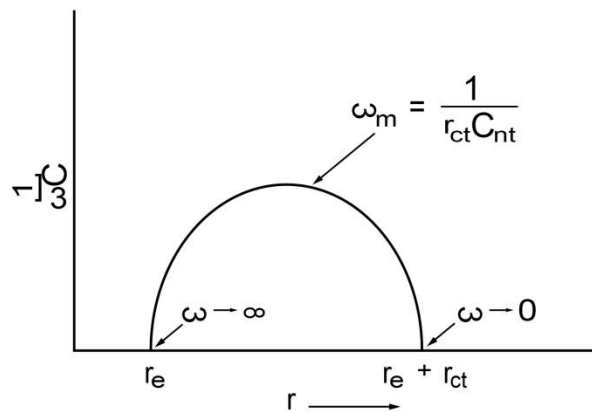
Figure 1.11: Complex plane analysis of cell impedance for a charge-transfer process with kinetic control at a planar electrode.[87]
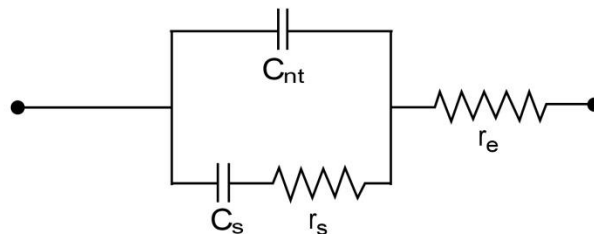
Figure 1.12: Equivalent circuits for a cell where cell impedance is kinetically controlled and is localized at working electrode by using a large, non-polarized counter electrode.[87]

Establishment of equivalent circuits to describe electrode processes with the faradaic impedance of diffusion-controlled processes at a planar electrode is referred to as the

''Warburg impedance.''[90] The double-layer capacitance have influence on the impedance of the electrode interface and derived an expression for its effect. A technique was developed to the study of electrode kinetics, [91, 92] with emphasis on the charge-transfer process.

The charge-transfer step has been considered and analyzed for coupled homogeneous and heterogeneous chemical reactions. Adsorption processes can be studied by this technique, that analyses the solid / solution interface by equivalent circuitry to calculate the interfacial resistance, capacitance, and inductance and relates these to reaction mechanisms.

The system without adsorption and complications of homogeneous series reactions where the impedance can be represented by a circuit diagram as shown in Figure 1.12. Where, C_{nf} is Nonfaradic capacitance; C_s, r_s is faradic components of impedance; r_e *is* electrolyte resistance. In this analysis, the electrode process is evaluated by the analytical technique of complex plane analysis. Here the capacitive component $1/(\omega C)$ is plotted versus the resistive component of the cell. Figure 1.11 shows a typical plot, which displays kinetic control only.
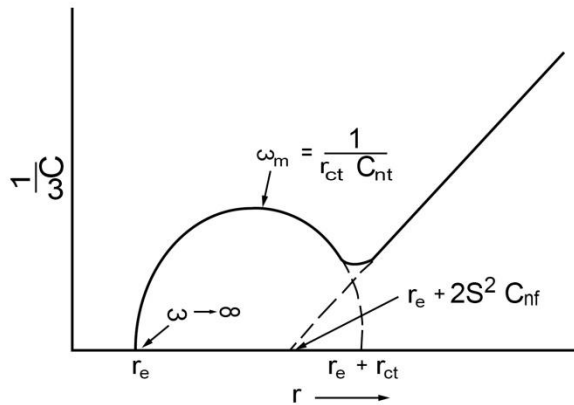
Figure 1.13: Complex plane analysis of cell impedance for a charge-transfer process with both kinetic and diffusion control at a planar electrode.[87]

The interdependence of the capacitive and resistive components yields a semicircle, with the top yielding the charge-transfer resistance r_{ct},

$$r_{ct} \, C_{nf} = \frac{1}{\omega_o}$$

where C_{nf} is the nonfaradaic capacitance and $r_{ct} = RT/nF(i_o)_{app}$. The intercept of the semi-circle and the abscissa gives the electrolyte resistance r_e and again r_{ct}. If the electrode

process is governed by both kinetic and diffusion control, a somewhat different plot is observed, as shown in Figure 1.13.

In this plot, the linear portion of the curve corresponds to the process where diffusion control is predominant. From this plot, in addition to the previously mentioned measurement, the extrapolated linear portion gives a somewhat complex expression involving the diffusion coefficients of the oxidized and reduced species,

$$\text{Intercept} = r_e + 2\, S^2\, C_{nf}$$

Where, $S = \dfrac{RTL}{n^2 F^2 \sqrt{2}}$ and $L = \dfrac{1}{C_o \sqrt{D_o}} + \dfrac{1}{C_R \sqrt{D_R}}$

D_o being the diffusion coefficient of the oxidized species and D_R that of the reduced species.

Treatment of this system assumes that we can write the equivalent circuit of kinetic and diffusion control as shown in Figure 1.14, where the diffusion component of the impedance is given by the Warburg impedance W.
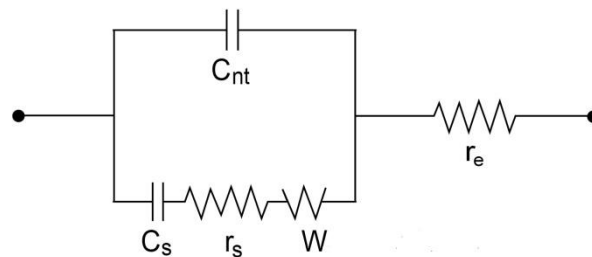
Figure 1.14: Equivalent circuit for an electrode process limited by both charge-transfer kinetics and diffusion processes. The diffusion portion of the impedance is represented by the Warburg impedance.[87]

The AC impedance technique coupled to the complex plane method of analysis is a powerful tool to determine a variety of electrochemical parameters.

This technique has found considerable acceptance in measuring fast rate constants, and it has been extended to include faradaic rectification and second-harmonic generation and detection. These advanced techniques extend the range of AC impedance measurements to the evaluation of charge-transfer rate constants with values of 10 cm/s or greater. In addition to applications in characterization of battery electrode reactions, as well as for a simple nondestructive check of the state of charge of batteries [93, 94]. This method is

therefore finding increasing utility in the study of battery systems. EIS is a powerful tool to evaluate battery electrode materials and has recently been shown to describe ion intercalation electrodes [95] and provide rate constants for the respective electrode processes.

1.9 Objectives of the Present Work

The objectives of this research are to develop a zinc/aluminum ion battery and also to study the galvanostatic charge-discharge capacity, cyclic stability, coulombic efficiency, studying electrode processes involving change in electrical impedance using various electrochemical techniques.

The specific aims are:

i.   To synthesize graphene on pencil graphite electrode (GPGE) by cyclic voltametric method.

ii. To explore the potential application of GPGE as an electrode in Zn/Al ion battery,

iii. To characterize the battery using different electrochemical methods,

iv. To test and validate the battery for storing energy.

CHAPTER II

Literature Review

2.1 Introduction

A battery is a device that converts the chemical energy contained in its active materials directly into electric energy by means of an electrochemical oxidation-reduction (redox) reaction. In the case of a rechargeable system, the battery is recharged by a reversal of the process. This type of reaction involves the transfer of electrons from one material to another through an electric circuit. While the term ''battery'' is often used, the basic electrochemical unit being referred to is the "cell." A battery consists of one or more of these cells, connected in series or parallel, or both, depending on the desired output voltage and capacity.

2.2 Advancements of Zinc/Aluminum ion battery in aqueous system

In recent days, aqueous rechargeable batteries have become interest of extensive research, which are inherently safe by avoiding flammable organic electrolyte solutions. Moreover, aqueous electrolytes are not expensive, and the assembly process of the batteries is also easy. In addition, the ionic conductivity of aqueous electrolytes is high, about 2 orders of magnitude higher than those of organic electrolytes, which ensures high rate capability and, thus, high power density [11, 12].

Dipan Kundu *et al.* [16] developed of a high-capacity and long-life aqueous rechargeable zinc battery using a metal oxide intercalation cathode. Here a vanadium oxide bronze pillared by interlayer Zn^{2+} ions and water ($Zn_{0.25}V_2O_5.nH_2O$) was used as the positive electrode for a Zn cell. A reversible Zn^{2+} ion (de)intercalation storage process at fast rates, with more than one Zn^{2+} per formula unit (a capacity up to 300 mAhg^{-1}), is characterized. The Zn cell offers an energy density of ~450Whl^{-1} and exhibits a capacity retention of more than 80% over 1,000 cycles, with no dendrite formation at the Zn electrode.

Mylad Chamoun *et al.* [52] reported the fabrication and characterization of low cost, with significant reduction potential and relative safety of the zinc electrode as a reductant in secondary batteries. They exploit such a shape change for the benefit of static electrodes through the electrodeposition of hyper-dendritic nanoporous zinc foam. Electrodeposition

of zinc foam resulted in nanoparticles formed on secondary dendrites in a three-dimensional network with a particle size distribution of 54.1–96.0 nm. The nanoporous zinc foam contributed to highly oriented crystals, high surface area and more rapid kinetics in contrast to conventional zinc in alkaline mediums. The anode material presented had a utilization of ~88% at full depth-of-discharge (DOD) at various rates indicating a superb rate capability. The rechargeability of Zn/Zn^{2+} showed significant capacity retention over 100 cycles at a 40% DOD to ensure that the dendritic core structure was imperforated. The dendritic architecture was densified upon charge–discharge cycling and presented superior performance compared with bulk zinc electrodes.

Faxing Wang *et al.* [53] reported, an aqueous rechargeable zinc//aluminum ion battery with good cyclic performance on the basis of zinc as the negative electrode and ultrathin graphite nanosheets as the positive electrode in an aqueous $Al_2(SO_4)_3/Zn(CH_3COO)_2$ electrolyte. The positive electrode material was prepared through a simple electrochemically expanded method in aqueous solution. The average working voltage of this aqueous rechargeable battery is 1.0 V, which is higher than those of most rechargeable Al ion batteries in an ionic liquid electrolyte. It could also be rapidly charged within 2 min while maintaining a high capacity. Moreover, its cycling behavior is also very good, with capacity retention of nearly 94% after 200 cycles.

S. Liu *et al.* [55] prepared Copper hexacyanoferrate (CuHCF) nanoparticles with Prussian blue structure via a simple coprecipitation method, which present the cathodic ability to insert Al ions reversibly in aqueous solution. CuHCF is verified to be a promising cathode material for aqueous Al-ion batteries. The discharge mid-potential is 0.54 V (vs. SCE), making CuHCF appropriate as cathode materials for aqueous aluminum ion battery. Cycle performance test is conducted at the current density of 400 mA g-1. The maximum discharge capacity reaches 41.0 mAh g^{-1} at the second cycle. Then, the capacity is gradually decreased to 22.5 mAh g^{-1} after 1000 cycles with retention of 54.9%.The capacity loss may be due to the dissolution of CuHCF in the acidic aqueous $Al_2(SO_4)_3$ solution.

2.3 Advancements of Aluminum ion battery in non-aqueous system/ionic liquids

The development of the batteries based on nonflammable electrolytes of low toxicity is critical for minimizing safety hazard and environmental impact. For this reason, ionic liquids (ILs) have been investigated for energy storage due to their low vapor pressure and wide electrochemical windows, unfortunately with the caveat of high cost in most cases. A new class of ionic liquids, referred to as ionic liquid analogs (ILAs) or so-called deep eutectic solvents, generally formed through a mixture of a strongly Lewis acidic metal halide and Lewis basic ligand, have gained significant attention due to their comparable electrochemical and physical properties with reduced cost and minimal environmental footprint.

Wei Wang et al. [6] proposed a Inew cathode material for super-valent battery based on aluminium ion intercalation and deintercalation where VO_2 and high-purity Al foil are used as cathode and anode respectively. First-principles calculations are also employed to theoretically investigate the crystal structure change and the insertion-extraction mechanism of Al ions in the super-valent battery. Long cycle life, low cost and good capacity are achieved in this battery system. At the current density of 50 mAg^{-1}, the discharge capacity remains 116 mAhg^{-1} after 100 cycles. Comparing to monovalent Li-ion battery, the super-valent battery has the potential to deliver more charges and gain higher specific capacity.

Haobo Sun et al. [96] proposed and established a new kind of Al-ion battery with carbon paper as the cathode, highpurity Al foil as the anode and ionic liquid as the electrolyte. The significance of the presented battery is going to be an extremely high average voltage plateau of ca. 1.8 V vs. Al^{3+}/Al. As an Al-ion full battery, this is the first time that such a high voltage plateau has been reported. Even discharged at 100 mA g^{-1}, the capacity can reach as high as 69.92 mA h g^{-1} over 100 cycles with high reversibility. Due to the low cost and abundance of raw materials (aluminium and graphite), the Al-ion battery established in this work shows bright prospect in the commercial application of Al-ion batteries.

Handong Jiao et al. [97] assembled a new Al-ion battery based on an affordable and nontoxic liquid electrolyte made from molten AlCl$_3$/urea. As the cathode material, natural graphite shows two well-defined discharge voltage plateaus at about 1.9 and 1.5 V with a high specific capacity of 93 mA h g^{-1} and excellent coulombic efficiency (~99%). The

attractive capacity (about 78 mAhg^{-1}) is retained even at a high current density of 1000 mA g^{-1}. Moreover, no faster fading in capacity is observed after 500 cycles. This electrolyte could provide a new system for Al ion batteries, which can be used for large scale energy storage, owing to its cost advantages, high-rate capability and durability.

Kostiantyn V. Kravchyk *et al.* [98] reported efficient aluminum chloride−natural graphite battery by probing the recently proposed aluminum−ionic liquid−graphite architecture. Using ^{27}Al nuclear magnetic resonance, they confirmed that AlCl$_4^-$ acts as an intercalating species. Although previous studies have focused on graphitic cathodes, we analyzed the practicality of achievable energy densities and found that the AlCl$_3$-based ionic liquid is a capacity-limiting anode material. By focusing on both the graphitic cathode and the AlCl$_3$-based anode, they improved the overall energy density. First, high cathodic capacities of ≤150 mAh g^{-1} and energy efficiencies of 90% at high electrode loadings of at least 10 mg cm^{-2} were obtained with natural, highly crystalline graphite flakes, which were subjected to minimal mechanical processing. Second, the AlCl$_3$ content in the ionic liquid was increased to its maximal value, which essentially doubled the energy density of the battery, resulting in a cell-level energy density of ≤62 Wh kg^{-1}. The resulting batteries were also characterized by high power densities of at least 489 W kg^{-1}.

Michael Angella *et al.* [99] developed a high Coulombic efficiency (~99.7%) Al-ion battery is using earth-abundant aluminum as the anode, graphite as the cathode, and a cheap ionic liquid analog electrolyte made from a mixture of AlCl$_3$ and urea in a 1.3:1 molar ratio. The battery displays discharge voltage plateaus around 1.9 and 1.5 V (average discharge = 1.73 V) and yielded a specific cathode capacity of ~73 mAh g^{-1} at a current density of 100 mA g^{-1} (~1.4 C). High Coulombic efficiency over a range of charge–discharge rates and stability over ~150–200 cycleswas easily demonstrated. In situ Raman spectroscopy clearly showed chloroaluminate anion intercalation/deintercalation of graphite (positive electrode) during charge–discharge and suggested the formation of a stage 2 graphite intercalation compound when fully charged. Raman spectroscopy and NMR suggested the existence of AlCl$_4^-$, Al$_2$Cl$_7^-$ anions and [AlCl$_2$·(urea)$_n$]$^+$ cations in the AlCl$_3$/urea electrolyte when an excess of AlCl$_3$ was present. Aluminum deposition therefore proceeded through two pathways, one involving Al$_2$Cl$_7^-$ anions and the other involving [AlCl$_2$·(urea)$_n$]$^+$ cations. This battery is a promising prospect for a future high-performance, low-cost energy storage device.

Di-Yan Wang *et al.* [100] reported an advanced aluminium ion battery cell made of high-quality pristine natural graphite flakes which achieved a specific capacity of ~110 mAh g^{-1} with Coulombic efficiency ~98%, at a current density of 99 mAg^{-1} (0.9 C) with clear discharge voltage plateaus (2.25–2.0 V and 1.9–1.5 V). The cell has a capacity of 60 mAhg^{-1} at 6 C, over 6,000 cycles with Coulombic efficiency ~99%. Raman spectroscopy shows two different intercalation processes involving chloroaluminate anions at the two discharging plateaus, while C–Cl bonding on the surface, or edges of natural graphite, is found using X-ray absorption spectroscopy. Finally, theoretical calculations are employed to investigate the intercalation behaviour of choloraluminate anions in the graphite electrode.

D. Gelman *et al.* [101] presented a novel non-aqueous Aluminum–air battery based on an ionic liquid electrolyte. Al anode high corrosion rate in aqueous alkaline solution is of major concern in terms of Al usage and safety. In non-aqueous electrolytes adverse Al surface activation substantially limits any power output. In this study battery utilized 1-ethyl-3-methylimidazolium oligo-fluoro-hydrogenate (EMIm(HF)$_{2.3}$F) room temperature ionic liquid (RTIL). Al–air batteries can sustain current densities up to 1.5 mA/cm^2, producing capacities above 140 mAh/cm^2, thus utilizing above 70% of the theoretical Al capacity. This is equivalent to an outstanding energy densities of 2300 W h kg^{-1} and 6200 W h L^{-1}. They detected Al$_2$O$_3$ at the air electrode as the battery discharge product of the oxygen reduction coupled with Al ions migrated to the air electrode.

Leyuan Zhang *et al.* [102] reported a low-cost and high-energy hybrid iron-aluminum liquid battery achieved by deep eutectic solvents. This work demonstrated a low-cost, high-energy Fe-Al hybrid liquid battery that took advantage of the desirable properties of deep eutectic solvents (DESs). The strategy of additive enabled the full charging and discharging of the Fe-Al battery with long cycle life while the stable stripping and deposition of Al is achieved. Using Fe(210) catholyte at a concentration of 5 M, the Fe-Al battery can deliver a high energy density of approximately 166 Wh L^{-1} with an average operating voltage of 1.41 V. Furthermore, by dissociating the iron complexes in Fe(126) DES, the Fe-Al battery could achieve the full charge and discharge over 60 cycles without degradation. Here, an all-DES-based liquid battery was proposed with an ultrahigh concentration of redox species, resulting in high energy density. The DES maintains reduced lattice energy and depressed freezing point and provides a new platform for developing green redox species based on new chemistry.

Meng-Chang Lin *et al.* [9] presented an ultrafast rechargeable aluminium-ion battery with high-rate capability that uses an aluminium metal anode and a three-dimensional graphitic-foam cathode. The battery operates through the electrochemical deposition and dissolution of aluminium at the anode, and intercalation/de-intercalation of chloroaluminate anions in the graphite, using a non-flammable ionic liquid electrolyte. The cell exhibits well-defined discharge voltage plateaus near 2 volts, a specific capacity of about 70mAh g^{-1} and a Coulombic efficiency of approximately 98 percent. The cathode was found to enable fast anion diffusion and intercalation, affording charging times of around one minute with a current density of 4,000 mAg^{-1} (equivalent to 3,000 Wkg^{-1}), and to withstand more than 7,500 cycles without capacity decay.

N. Jayaprakash *et al.* [7] reported a novel aluminium-ion rechargeable battery comprised of an electrolyte containing $AlCl_3$ in the ionic liquid, 1-ethyl- 3-methylimidazolium chloride, and a V_2O_5 nano-wire cathode against an aluminium metal anode. The battery delivered a discharge capacity of 305 mAh g^{-1} in the first cycle and 273 mAh g^{-1} after 20 cycles, with very stable electrochemical behaviour. The theoretical energy density of the Al-ion battery with V_2O_5 as the cathode against aluminium metal as the anode was determined to be 240 Wh kg^{-1}, which is not enough to power very much. But considering the other attractive attributes of an aluminium based secondary battery platform, the energy density of this first Al-ion cell is enough to initiate a global search for new materials and cell designs which we anticipate will lead to rapid and sustained improvements.

Huajun Tian *et al.* [103] reported rechargeable aluminum/iodine battery redox chemistry in ionic liquid electrolyte for the first time. The unique conversion reaction mechanism of the Al/I_2 battery chemistry avoided the cathode material disintegration during repeatedly charge/discharge process, and this system successfully suppressed the shuttle of dissolved polyiodide in ionic liquid because of the hydrogen-bonding interaction, resulting in a robust rechargeable RABs system. The rechargeable Al/I_2 battery based on the I_3^-/I^- redox chemistry demonstrated highly reversible in Al^{3+} ion storage, providing a high capacity of >200 $mAhg^{-1}$ at 0.2 C, and high stability for even over 150 cycles at 1 C. This work provided a new insight in designing RABs system based on redox chemistry.

Yingpeng Wu *et al.* [104] reported a novel three dimensional graphitic foams (3DGF) derived from chloroaluminate anion intercalation of graphite followed by thermal

expansion and electrochemical hydrogen evolution in the pores of graphitic sheets for ultrafast aluminum-ion battery. The charge and discharge cycles of an Al/3DGF battery at a high current density up to 12 Ag^{-1} exhibiting a typical voltage profile of the Al/graphite battery with the plateau at ~1.8 V a discharge capacity of ~60 $mAhg^{-1}$, and a coulombic efficiency of ~100% with excellent stability of ~100% capacity retention over ~4000 cycles. The Al/3DGF was also capable of rapid charging (at 12 Ag^{-1}) and slow discharging (down to 2 Ag^{-1}) with similar discharge capacity (~60 $mAhg^{-1}$) and a high coulombic efficiency. In a controlled experiment, when a 3DGF foam was placed with ~0.5 cm^2 scale graphitic sheets parallel to a current collector and compressed the foam to reduce its thickness and surface area, it was observed lower battery performance with a capacity of only ~30 mAh g^{-1} under a charge/discharge current density of 600 mA g^{-1} .

Xiaolong Zhang *et al.* [105] reported a novel aluminum–graphite dual-ion battery (AGDIB) in an ethyl–methyl carbonate (EMC) electrolyte with high reversibility and high energy density. It is the first report on using an aluminum anode in dual-ion battery. The battery shows good reversibility, delivering a capacity of ~100 mAh g^{-1} and capacity retention of 88% after 200 charge–discharge cycles at 2 C (1 C corresponding to 100 mA g^{-1}). To the best of our knowledge, performance of the battery is among the best of reported dual-ion batteries.

Chen Wang *et al.* [106] reported the electrochemical behavior of an aluminum alloy anode for rechargeable Al-ion batteries using an $AlCl_3$–urea liquid electrolyte. Due to its characteristics of high capacity, low cost, being non-flammable, and involving a three-electron redox reaction, the aluminum rechargeable battery has received wide attention. Because of these advantages, they focused on a low-cost aluminum alloy anode and detect the discharge/charge reaction mechanism in the aluminum chloride-urea liquid electrolyte at 110–130 $^{\circ}$ C. The discharge voltage of the battery is about 1.9 V and 1.6 V, and at the current density of 100 mA g^{-1} the cell can produce a specific capacity of ~94 mA h g^{-1}. Compared to the pure aluminum anode, the system has a promising future for high efficiency, low-cost energy storage devices.

Sung Chul Jung *et al.* [107] reported that the unique structural characteristic of graphitic foam, i.e., mechanical flexibility of few-layered graphene nanomaterials, plays a key role for the ultrafast aluminum-ion battery. They found that $AlCl_4^-$ is stored by forming doubly-stacked ionic layers in the interlayer space between graphene sheets and their

diffusivity increases dramatically once graphene film is less than five layers thick; the diffusivity begins to increase when the film thickness reduces below five layers in such a way that the film thickness of four, three, and two graphene layers enables 48, 153, and 225 times enhanced diffusivity than that of the bulk graphite, respectively, and this nanoscale thickness is mainly responsible for the observed ultrafast rate capability of graphitic foam. The faster anion conductivity with the reduced film thickness is attributed to high elasticity of few-layered graphene, providing more space for facile $AlCl_4^-$ diffusion. This study indicated that even bulky polyanions can be adopted as carrier ions for ultra-high rate operation if highly elastic few layered graphene was used as an active material.

Table 2.1: Materials used as cathode and anode in different Zn and Al-ion batteries and their electrochemical performances.

SL. No.	Cathode	Anode	Electrolytes	Capacity, mAh/g	C-rate, mA/g	Cyclic Stability	Discharge Voltage	Efficiency	Ref.
1	Graphite powder on Carbon Fiber Paper	High Purity Al-foil	$AlCl_3$-Urea (1.3/1 M)	~73	100	~150–200	1.73 V (vs. Al^{3+}/Al)	99.7%	[99]
2	Pristine Graphite flakes on Tungsten-plates	Al-foil	$AlCl_3$-EMIC	=150	100	~100	1.77 V (vs. Al^{3+}/Al)	90%	[98]
3	Round Carbon paper	High purity Al-foil	$AlCl_3$-EMIC (1.3/1 M)	69.9	100	Over 100	1.8 V (vs. Al^{3+}/Al)	100%	[96]
4	VO_2 pasted on S. Steel	High purity Al-foil	$AlCl_3$-Urea (1/1 M)	116	50	100	0.5 V		[6]
5	Graphite on Carbon Paper	Pure Al	$AlCl_3$-Urea (1.5/1 M) @120°C	~93	100	500	1.7 V	99%	[97]
6	Pristine Nat. graphite flakes	Al-foil (~20 μm)	$AlCl_3$-EMIC (1.3/1 M)	~110	99	6000 @ 60 mA/g	2.25-2.0 V & 1.9-1.5 V	98%@ 99mA/g	[100]
7	3D graphitic foam	Al-metal	$AlCl_3$-EMIC	~60	100	7500 @ 4 A/g	~2.0 V		[9]
8	V_2O_5 nanowires	Al-metal	$AlCl_3$-EMIC	273		~20	~0.45 V		[7]
9	Super P + Poly vinylidene fluoride binder on Ti surface	Al-strip attached on Cu-foil	Catholyte: $FeCl_3.6H_2O$/ Urea + Ethylene glycol Anolyte: $AlCl_3$/Urea+ Dichloroethane	41 mAh/mL	0.1 mA/cm²	Upto 60	1.41 V	100%	[102]
10	I_2 with PVP (Polymeric matrix)	Al-metal	$AlCl_3$-EMIC (1.3/1 M)	>200	13	150 @ 66 mA/g	~0.74 V		[103]
11	Pt-foil with Air (O_2)	Al anode	1-ethyl-3-methyl imidazolium oligo-fluoro-hydrogenate ($EMIm(HF)_{2.3}F$)	140 mAh/cm²	1.5 mA/cm²,	No info.	~1 V	70%	[101]
12	No Information	Al- alloy	$AlCl_3$-urea liquid at 110–130 °C.	~94	100		1.9 & 1.6 V	100%	[107]
13	3D-pyrolytic graphitic foil	Al-foil	$AlCl_3$-EMIC (1.3/1 M)	~60	2000	4000	~ 1.8 V	100%	[105]
14	Natural graphite+ carbon black(10%) + PVDF(10%) on Al	Al-metal	$LiPF_6$ (4M) in Ethyl methyl Carbonate	~100 @ 100 mA/g	200	200	4.2 V	88%	[106]
15	KCu[Fe(CN)$_6$]. 8H$_2$O	No Info.	$Al_2(SO4)_3$ in H_2O	41 (2nd)	400	1000	0.54 V	54.9%	[55]
16	Ultrathin Graphitic nanosheet	Zinc metal	$Al_2(SO4)_3$ + $Zn(CH_3COO)_2$ in H_2O	80	500	~200	1.0 V	94%	[53]
17	$Zn_{0.25}V_2O_5.nH_2O$ nanofibres	Zinc Metal	1.0M $ZnSO_4$ in water	300	300	1000	1.0 V	80%	[16]
18	Conventional Nickel electrode	Nanoporous zinc foam	8.9M KOH + 0.61M ZnO	328 mAh/g	166.7 mA/g	100	1.6 V vs $Ni(OH)_2$/NiOOH	40%	[52]

CHAPTER III

Procedure/ Methodology

3.1 Reagents and Materials

Nitric acid (HNO_3), aluminum Chloride ($AlCl_3$), zinc Acetate ($Zn(CH_3COO)_2$), hydrochloric Acid (HCl), potassium chloride (KCl) were purchased from Merck, Germany. Pencil Graphites (Artline, 6B, 3.5 mm radius) and Zinc rod (5 mm radius) were purchased from local market supplier. Glass fiber paper (GFP) separator was bought from Sigma Aldrich, USA.

3.2 Equipment and Instruments

Cyclic voltammetry (CV) measurements were performed using a potentiostat/ galvanostat (Dropsens, µStat 8400) in a three electrode configuration, where GPGE, Ag/AgCl (in 3M KCl) and Pt-wire were used as working, reference and counter electrode repectively. Galvanostatic charging/discharging, chronopotentiometry, coulombic efficieny determination, electrochemical impedance spectroscopy (EIS) were performed using an electrochemical workstation (Biologic, SP-300). FT-IR spectroscopy was performed using IRTracer1000 (Shimadzu, Japan). Characterization for SEM and EDX were performed by Jeol Scanning Electron Microscope (JSM-5510) and INCA Energy Dispersive X-ray Spectroscopy Detector, respectively.

3.3 Preparation of Graphene Coated Pencil Graphite Electrodes (GPGE)

A pencil graphite electrode (PGE) was treated electrochemically in 5.0M nitric acid solutions to produce graphene by CV over a potential range of -1.0 and +1.9V for 20 cycles with a 50 mV/s scan rate at room temperature to produce 20 layers of graphene coating on the pencil graphite electrode and denoted as GPGE. The graphene oxide coated graphite electrode is also called as GOPGE. In the electrochemical measurements, a classical three-electrode cell was used with a PGE working electrode, a Pt auxiliary electrode and an Ag/AgCl reference electrode. The working electrodes were washed with deionized water to remove impurities and dried at room temperature before the electrochemical experiments. Finally, the GPGE was washed with deionized water and was heated at 120 °C for 1 h to remove the moisture content.

3.4 Spectroscopic and Electrochemical Characterization of the Electrodes

FT-IR analysis of electrodes was performed using attenuated total reflectance (ATR) technique for of each the electrodes. The significance of CV in production of GPGE was investigated by synthesizing graphene oxide on pencil graphite electrode (GOPGE) in a potentiostatic method at +1.90V (vs. Ag/AgCl) for 5 min in 5.0M HNO_3. Then, GPGE and GOPGE were investigated by CV in a 0.1M KCl in potential range of –1.75V and +2.0V (vs. Ag/AgCl). EIS was carried out using an electrochemical workstation (Biologic SP-300) in the frequency range from 0.1 Hz to 1 MHz.
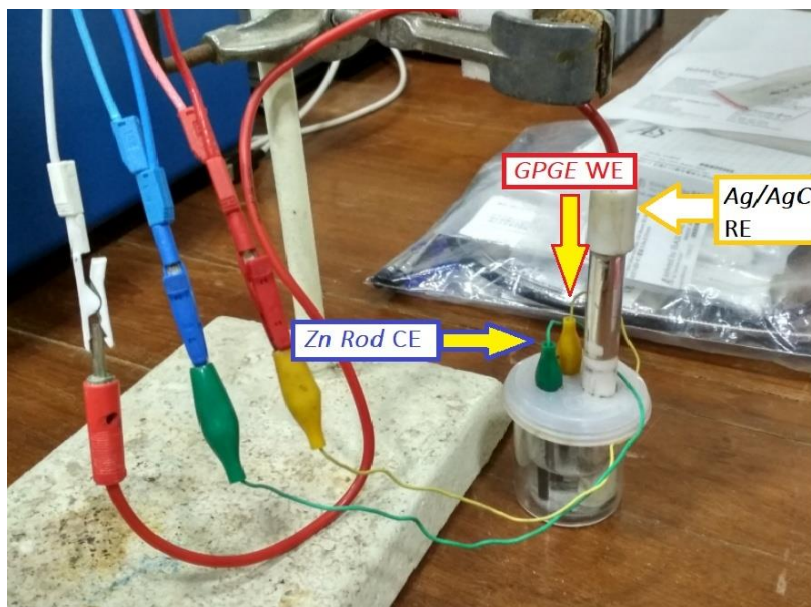
Figure 3.01: Experimental electrochemical cell setup.

3.5 Study of Energy Storage Behaviour

Characterization of battery performance was carried out in a three-electrode system using GPGE, Zn and Ag/AgCl as positive, negative and reference electrode, respectively in an aqueous $AlCl_3$/$Zn(CH_3COO)_2$ (0.5/0.5 M) electrolyte. The two electrodes were separated by a GFP separator and copper alligator clips were used as the current collector. Galvanostatic cycling studies were performed using a multichannel Biologic (SP-300) science instrument. As the highest capacity of 55.5 $mAhg^{-1}$ was achieved at a moderate current density of 50 mAg^{-1}, a current density of 55 mAg^{-1} was defined as the 1C rate and the remainder of the current rates was defined relative to this value. All tests were carried out at room temperature and N_2 gas was purged into the cell before starting the experiment to create an inert atmosphere and to make the electrolyte oxygen free.

Results and Discussion

4.1. Preparation of GPGE

CV for the preparation of graphene coated pencil graphite electrode (GPGE), possible formation mechanism of GPGE, electrochemical behaviors of GPGE and graphene oxide coated pencil graphite electrode (GOPGE) are shown in Figure 4.01, 4.02 and 4.03, respectively.
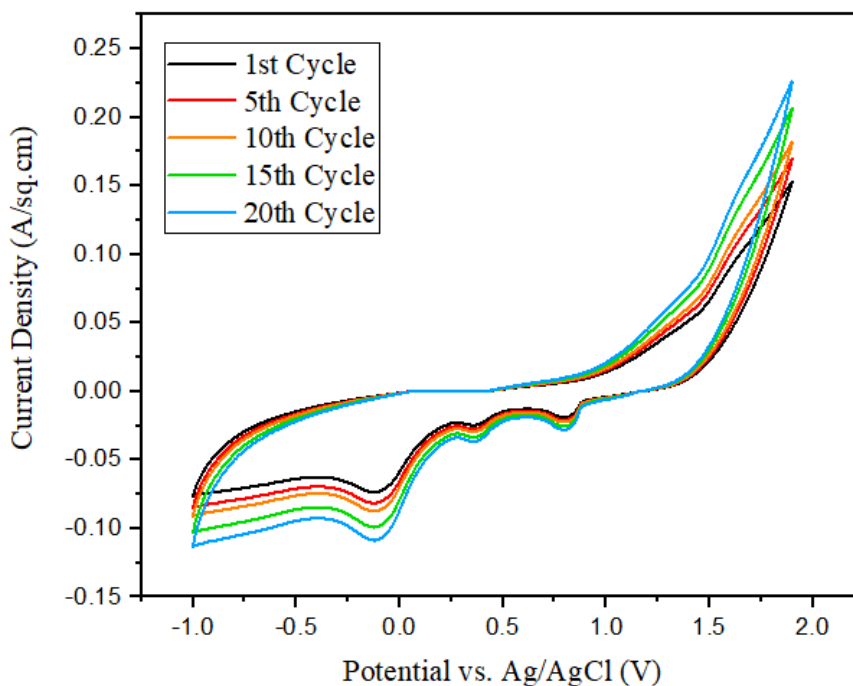
Figure 4.01: CVs of PGE in 5.0 M HNO_3 at 50 mV/s (20 cycles).

The electrochemical behaviors of the pencil graphite electrode (PGE) were investigated by CV in 5.0 M nitric acid (HNO_3) solution to find the optimum anodic and cathodic peaks in a three–electrode cell using PGE, Ag/AgCl and platinum wire as the working electrode (WE), counter electrode (CE) and reference electrode (RE), respectively. During the potential sweep in the potential range of –1.0 V and +1.90V (vs. Ag/AgCl), one oxidation peak and three reduction peaks were observed in the same solution. Figure 1(a) shows the 1st, 5th, 10th, 15th and 20th cycles in the CV of pencil graphite electrode (PGE) in 5.0 M

HNO_3 solution. Applying a positive potential sweep to the device produced a large amount of bubbles on the PGE. The main oxidation peaks were observed at +1.25 V and +1.64 V (vs. Ag/AgCl). Increase of anodic current at +1.25 V represents electrolysis of water by oxidation of O^{2-} ions into O_2 gas at PGE WE (*equation 1*) [108]. During this stage, the produced oxygen gas causes exertion of huge forces on the graphitic layer accompanied by oxidation into PGE surface having oxygen containing groups. Under high potential (at +1.64 V), further oxidation caused conversion of oxygen containing groups on PGE into graphene oxides (*equations 2 and 3*) [84].

Reactions during forward potential sweep:

$$2H_2O \longrightarrow O_2 + 4H^+ + 4e^- \tag{1}$$

$$4C_x + O_2 \longrightarrow 2C_xO$$

$$or, 4C_x + 2H_2O \longrightarrow 2C_{2x}O + 4H^+ + 4e^-$$

$$C_xOH \longrightarrow C_xO + H^+ + e^- \tag{2}$$

$$(C_xO)_2 + H_2O \longrightarrow C_{(2x-2)}COCOOH + H^+ + e^- \tag{3}$$
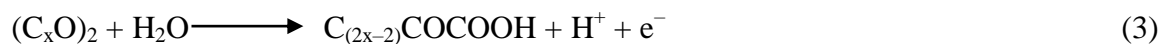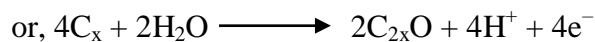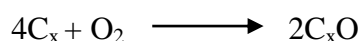
During reverse potential sweep from +1.90V to –1.0 V, peaks at +0.70, +0.35 and –0.15 V can be attributed to the reduction of graphene oxide to graphene.[84] These peaks correspond to reduction of graphene oxide to graphene on the PGE surface *(equation 4)* [77, 108]. Besides this, the reduction of NO_3^- anions produces NO and NO_2 gases (*equations 5 and 6*) at +0.70 V and +0.35 V, respectively at PGE surface.[49, 108] These gaseous species (NO and NO_2) can produce large forces on the graphite layers, which can expand the interlayer distance between the graphitic or graphene layers (Figure 4.02).

Reactions during reverse potential sweep:

$$C_{(2x-2)}COCOOH + H^+ + e^- \longrightarrow Graphene + H_2O \tag{4}$$

$$NO_3^- + 4H^+ + 3e^- \longrightarrow NO + 2H_2O \tag{5}$$

$$NO_3^- + 2H^+ + e^- \longrightarrow NO_2 + H_2O \tag{6}$$

As shown in Figure 4.02, NO_3^- ions together with H_2O molecules intercalate into the graphitic layers (positive electrode) and during this stage, oxidation of water produces O_2. Besides, oxygen–containing functional groups such as hydroxyls, carbonyls and epoxies undergo through further oxidation of the graphitic surface of PGE (*equations 2 and 3*). [109]
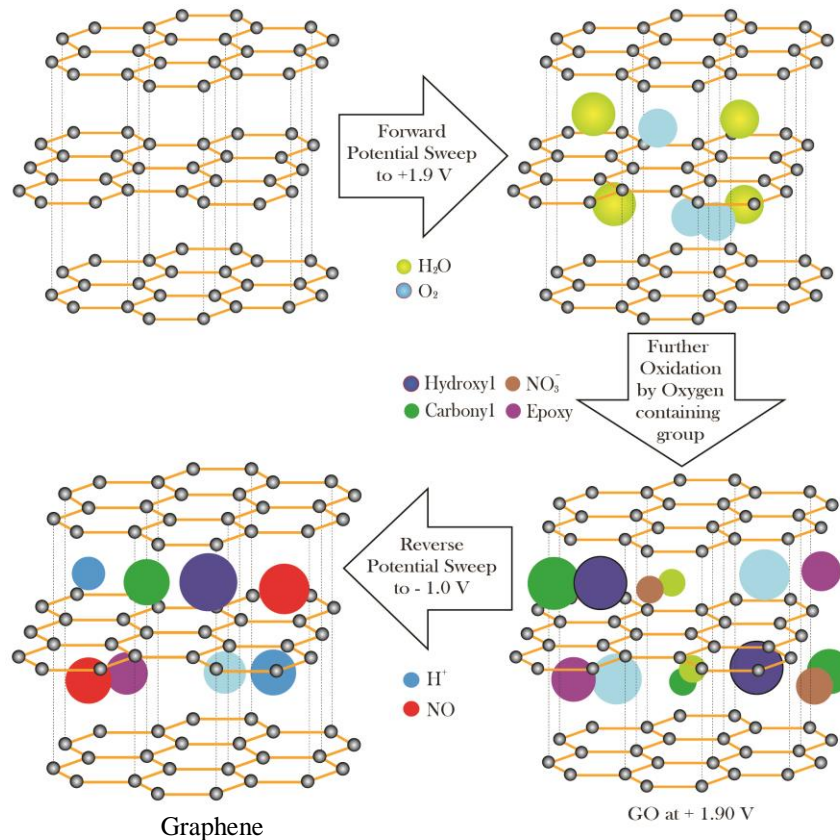
Figure 4.02: Possible formation mechanism of GPGE from PGE by CV in 5.0 M HNO_3 solution.

The anodic and cathodic peak intensities were related to the number of graphene layers produced on the PGE, which increased with increasing cycles. Since the electrical conductivity of graphene is greater than that of graphite or graphene oxide, a higher peak current intensity was obtained in the production of graphene layers on PGE during CV. The surface area of the electrodes is studied to be increased due to formation graphene layers. Although the given geometrical surface areas for both PGE and GPGE were same (0.10 cm^2), electrochemically active surface areas were calculated to be 1.1 cm^2 and 6.46 cm^2, respectively, using Randles–Sevcik *equation (7)* in 1.0 M KCl/1.0 mM $K_3Fe(CN)_6$ solution,

$$I_p = 0.4463 \text{ nF} \sqrt{\frac{nFD}{RT}} \text{ AC} \sqrt{v} \qquad (7)$$

Where i_p: the peak current, n: the number of electrons, F: Faraday constant, T: the temperature in Kelvin, R: the gas constant, A: the surface area of the working electrode (WE), D: the diffusion coefficient of the electroactive species (D = 7.7 x10^{-6} cm^2/s), C: the bulk concentration of the electroactive species and *v*: the scan rate of voltammograms.

The effects and importance of CV on the production of GPGE were also investigated. In this process, graphene oxide on the pencil graphite electrode (GOPGE) was synthesized by means of a potentiostatic method at +1.90V (vs. Ag/AgCl) for 5 minutes in 5.0M nitric acid solution.
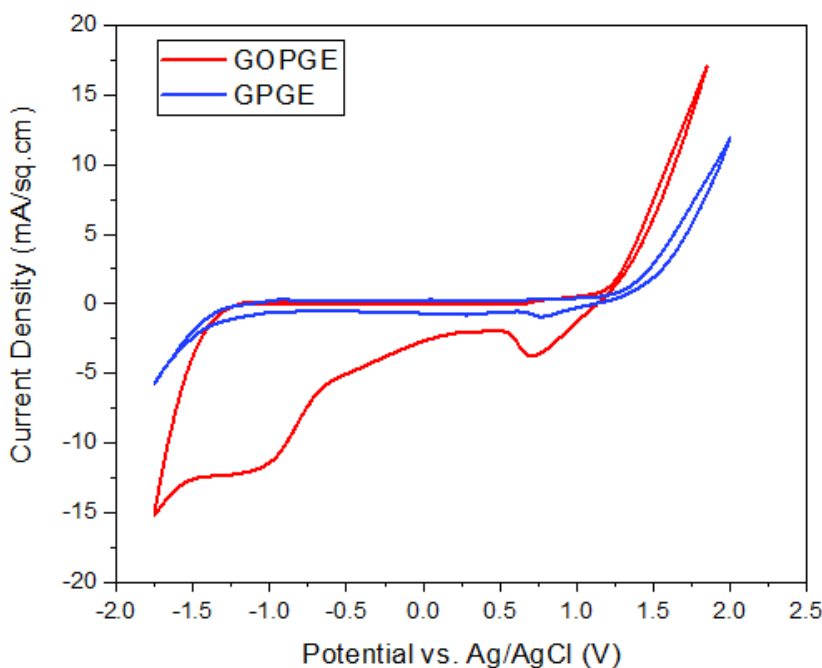
Figure 4.03: Electrochemical behaviors of GPGE and GOPGE in 0.1M KCl solution.

Then, CV was performed to investigate GPGE and GOPGE in 0.1M KCl electrolyte solution over the potential range of −1.75V and +2.0V (vs. Ag/AgCl) (Figure 1c). Although obvious reduction peaks for GPGE were not observed, two certain reduction peaks were observed at +0.75 V and −1.0 V for GOPGE. This result can be explained by the reduction of oxygen containing groups on GOPGE. Since GPGE has no oxygen containing groups, no reduction peaks were observed, as expected. According to this result, the graphene oxide (GO) formed at the anode was reduced to graphene at the cathode in same solution [84]. Figure 4.03 shows the cyclic voltammograms of GPGE along with no observed reduction peaks.

To ensure the formation of graphene oxide on pencil graphite (PG) in the forward potential sweep, the CV was performed by running negative potential sweep (reduction) first from +1.9 V to –1.0 V and then followed by running positive potential sweep (oxidation) in the reverse scan from –1.0 V to +1.9 V (1st cycle of Figure 4.04).
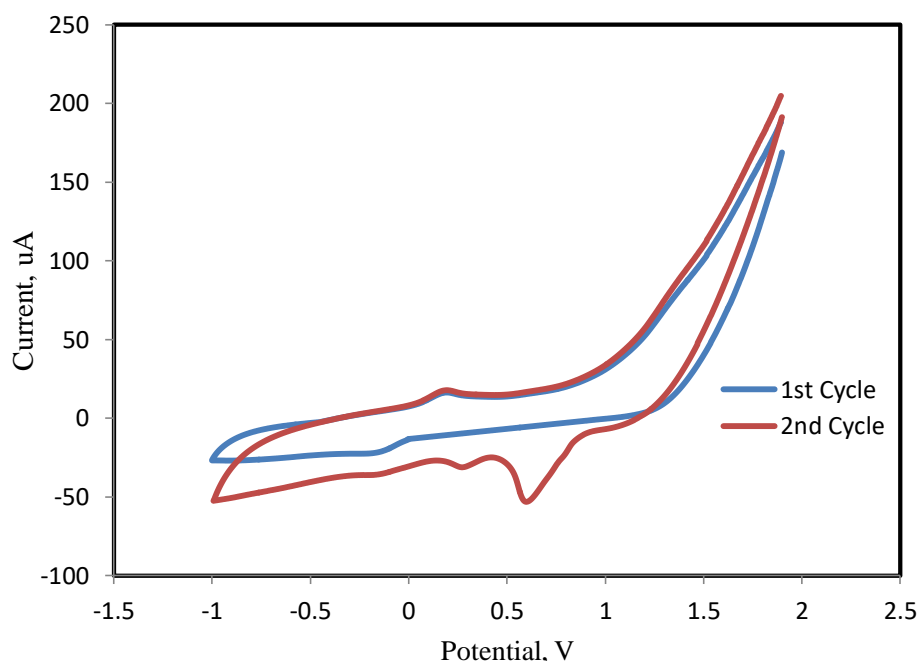
Figure 4.04: CV of PGE in 5.0M HNO_3 starting first with negative potential sweep.

It shows that there are no prominent reduction peaks indicating the absence of oxidized graphite or oxygen containing groups in raw PGE. However, in the 2nd cycle there occurs appearance of reduction peaks which reveals the production of graphite oxide only in the forward scan of the 1st cycle at around +1.45 V. These results verify the formation of graphene oxide in forward sweep and also prove that reduction peaks are not due to any other groups or materials previously contained in the PG, rather prior to oxygen containing groups formed in the positive (oxidizing) sweep of CV.

4.2 Characterization of GPGE by FT-IR Spectroscopy Analysis

FT-IR spectra of PGE, GOPGE and GPGE are shown in Figures 4.05, 4.06 and 4.08, respectively. The small peaks at 2915.58 and 2858.5 cm^{-1} indicating due to the presence of alkane stretching (from wax) in the graphite structure can be seen in the spectra of PGE (Figure 4.05).
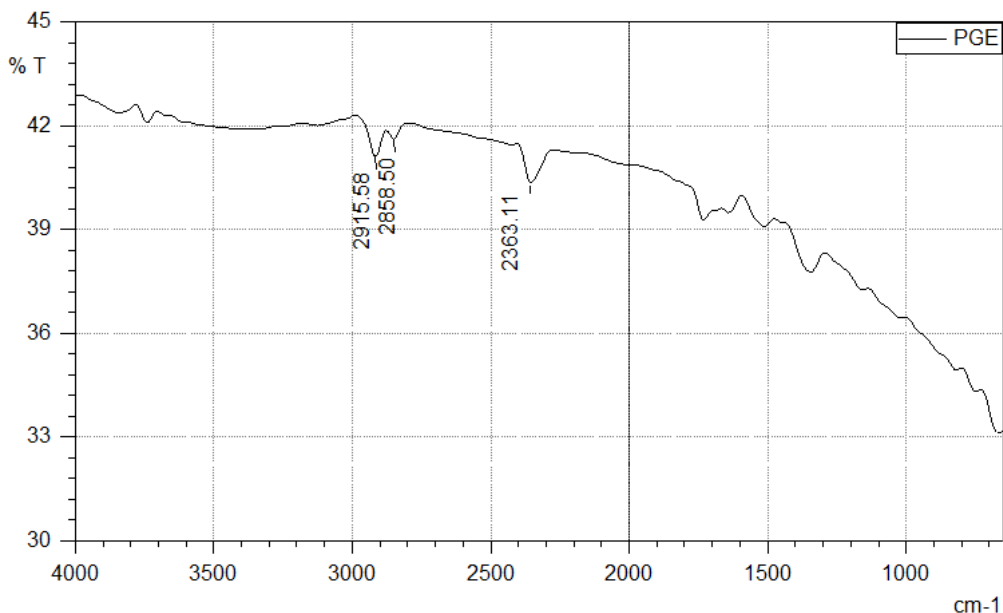
Figure 4.05: FT–IR spectra of Pencil graphite electrode (PGE).

Table 4.1: Wave-numbers (IR values) for bond vibrations in different functional groups of GOPGE.

Absorption at wave-number (cm^{-1})	Groups Present
3404.36, 3358.07, 3217.27	C-O–H, -CO-O–H, H bonded -O–H etc.
2922.16, 2860.43	C–H Stretching
1736, 1653	C=O, COOH
1577.77	sp^2 hybridized C=C in plane Stretching
1276.88	C–O–C bonds in epoxy groups
1064.7 (1300-100 cm^{-1})	C–O (alcohol, ether, carboxylic groups etc.)

The peaks obtained 3404.36, 3358.07 and 3217.27 cm^{-1} in FT-IR spectra (Figure 4.06) can be attributed to the oxygen hydrogen bond vibrations (hydroxyl groups) of C–O–H and CO–O–H on the surface of GOPGE (Figure 4.07 **A**).

42
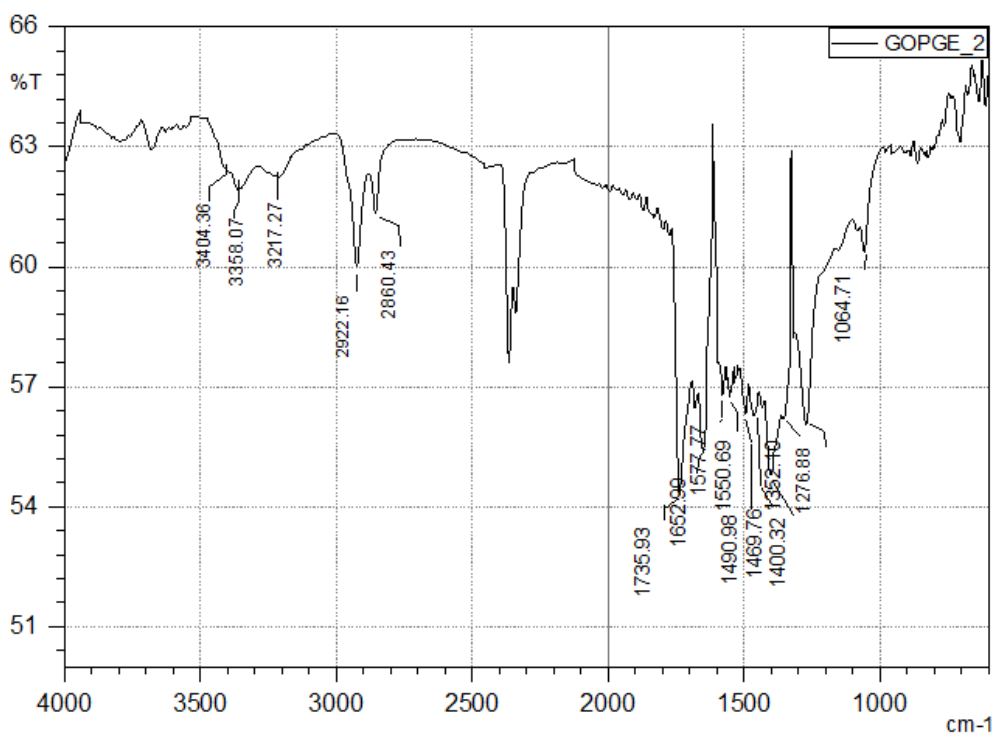
Figure 4.06: FT–IR spectra of Graphene oxide coated pencil graphite electrode (GOPGE).

The peaks of carbon oxygen bond vibrations from C=O and COOH could be seen at 1736, 1653 cm^{-1} (Figure 4.07 **B)**. The small peak at around of 1276.88 cm^{-1} is observed due to the presence of epoxy (C–O–C) groups (Figure 4.07 **C)**. Peaks obtained in between of 800–1330 cm^{-1} are also proves for the formation of C–O groups on the GOPGE [110].
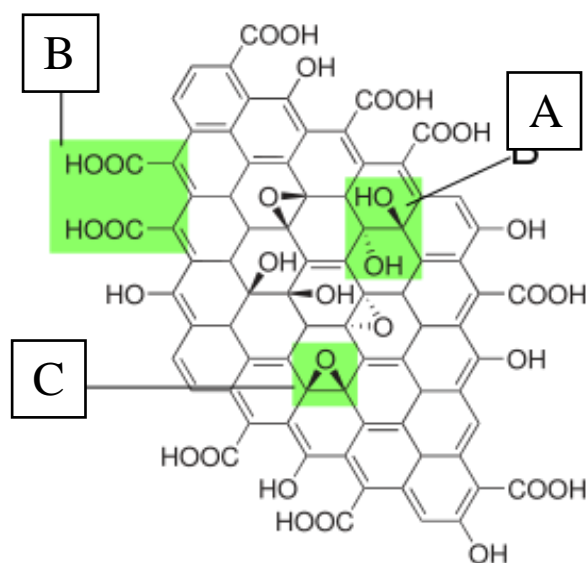
Figure 4.07: Proposed Structure of Graphene Oxide with functional groups.

A: Hydroxyl groups, **B**: Pairwise carboxyl groups, **C**: Epoxy bridges.[111]

According to above FT–IR analysis, a probable mechanism for graphene formation on PGE can be given as Eq. (8) and (9).

1st step: Forward potential sweep

Oxidation: PGE $\longrightarrow$ GOPGE + aH$^+$ + be$^-$ (8)
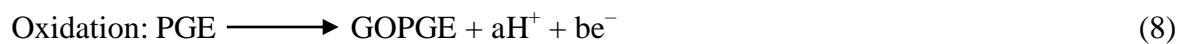
2nd step: Reverse potential sweep

Reduction: GOPGE + aH$^+$ + be$^-$ $\longrightarrow$ GPGE + cH$_2$O (9)
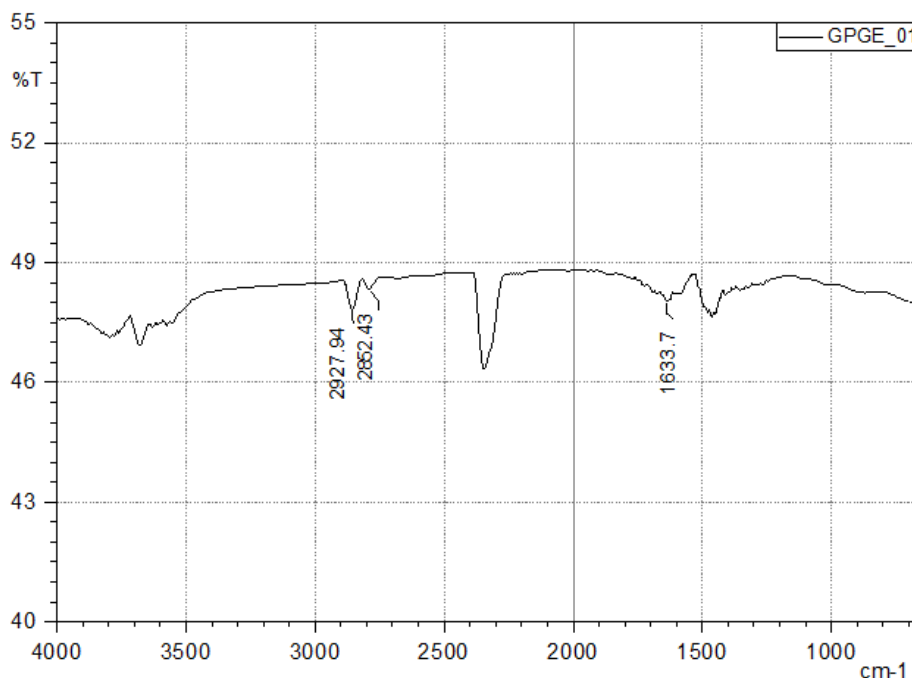
Figure 4.08: FT-IR spectra of graphene coated pencil graphite electrode (GPGE) over 20

The spectra of GPGE are almost same as that of PGE. Absorption peaks at 2928 and 2862.4 cm^{-1} can be related to C-H stretching where the small peak (1633.7 cm^{-1}) of C=C indicating the graphene structure could be seen in the spectra of GPGE (Figure 4.08).

4.3 Characterization of PGE and GPGE by Scanning Electron Microscopy (SEM)
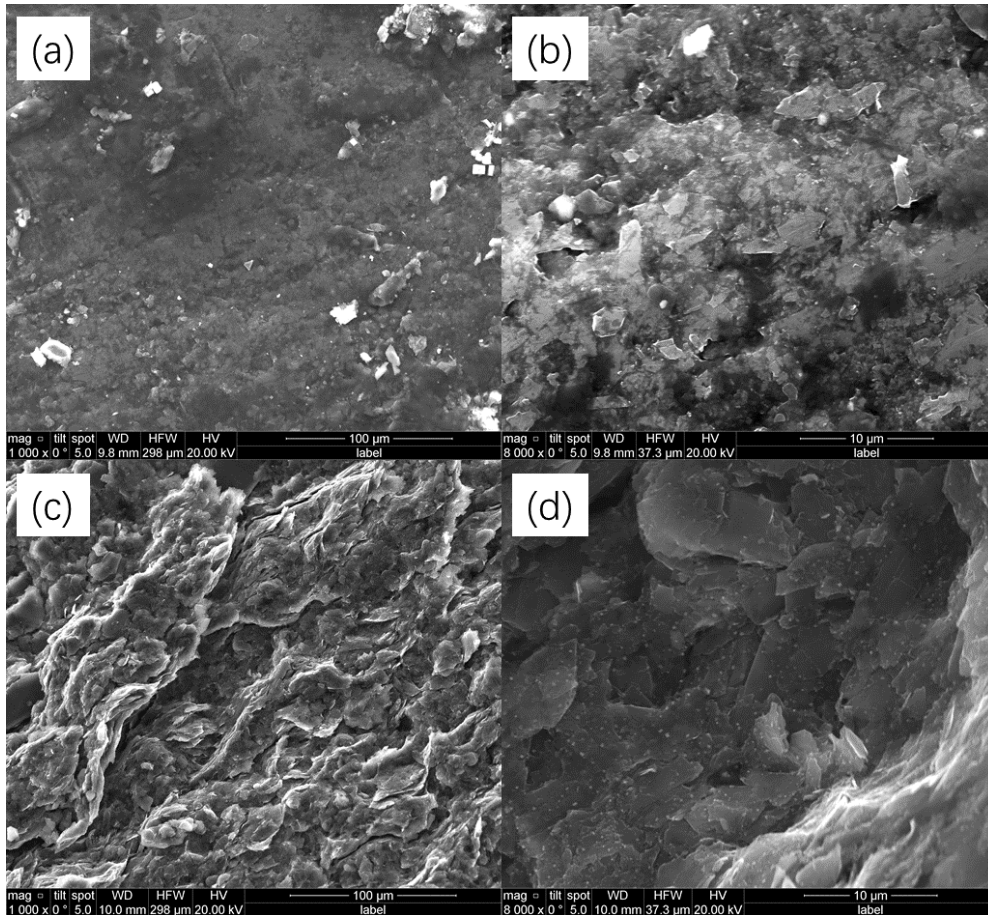
Figure 4.09: SEM images (a-b) of PGE and (c-d) of GPGE.

The morphologies of PGE and GPGE were explored using SEM. The SEM images of PGE (Figure 4.09 a-b) and GPGE synthesized by CV in 5.0M HNO_3 (Figure 4.09 c-d) show changes in the electrode surface. When SEM images of PGE surface are compared to that of GPGE surface, granular morphology was observed in for latter one (Figure 4.09 c-d) which exhibits the existence of graphene. The synthesis of graphene layers of GPGE showed better transparent optical properties to the electrode than that of PGE (Figure 4.09 a-b). This SEM analysis supports the synthesis of two dimensional (2D) ultrathin and flexible wrinkled structures of graphene layers on PGE.

4.4 Energy Storage Studies of Zn/Al-ion Cell

In order to explore the potential application of the GPGE as an electrode in Zn-Al ion battery, cyclic voltammetry, galvanostatic charge-discharge, cyclic stability and electrochemical impedance spectroscopy (EIS) measurements were performed in a three electrode configuration.

4.4.1 Investigation on Role of Electrolyte ions by Cyclic Voltammetry

Cyclic voltammograms of the Zn/Al-ion cell in 0.5M $Zn(CH_3COO)_2$, 1.5M KCl, 10^{-4} M HCl, $AlCl_3/Zn(CH_3COO)_2$ (0.5/0.5 M) solution are shown in Figure 4.10 in three electrode systems using GPGE, Zn metal and Ag/AgCl as WE, CE and RE, respectively.
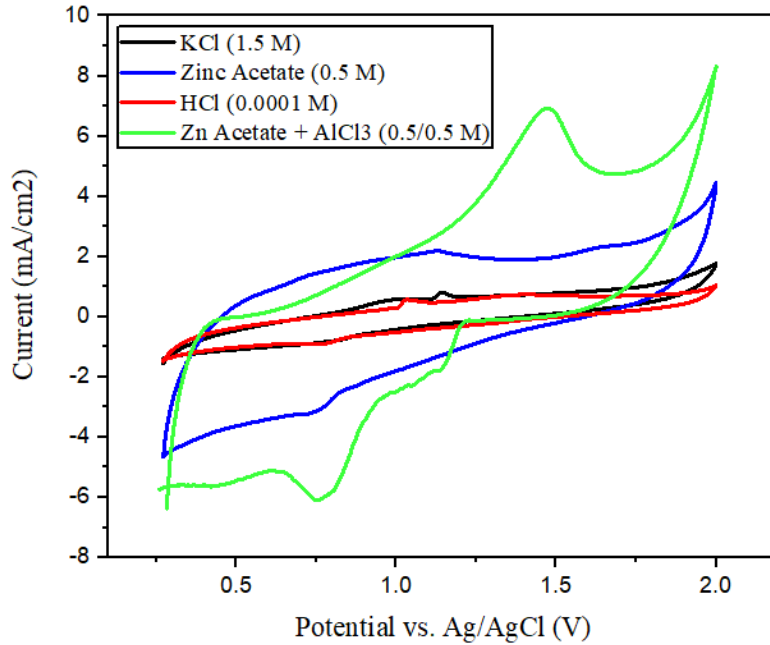
Figure 4.10: CV curves of GPGE in different electrolytes at 1 mV s^{-1}.

For Zn/Al-ion cell with GPGE positive electrode in $AlCl_3/Zn(CH_3COO)_2$ (0.5/0.5 M) solution, a pair of reversible redox peaks can be observed (Figure 4.10) clearly at +1.51 and +0.78 V (versus Ag/AgCl). But for 0.5 M $Zn(CH_3COO)_2$, it shows only a rectangular CVs with little redox characteristics. In a 1.5 M KCl electrolyte and 10^{-4} M HCl near the pH of $AlCl_3/Zn(CH_3COO)_2$ (0.5/0.5 M) solution, it presents an asymmetrical CV with no significant oxidation peak, suggesting poor reversibility of the redox reactions. From these results it could be suggested that the redox peaks enhances in the $AlCl_3/Zn(CH_3COO)_2$ electrolyte due to the presence of Al^{3+} or $[Al(H_2O)_6]^{3+}$ instead of Zn^{2+}, H^+, CH_3COO^-, or Cl^- ions. The redox peaks may be recognized as a result of Al^{3+} or $[Al(H_2O)_6]^{3+}$ ion intercalation and deintercalation into/ from the GPGE, which is similar to the behavior of graphite in ionic liquid electrolyte [9].

Reactions:

During positive potential sweep of CV using C_{3y} (GPGE) as WE (charging process):

Oxidation (deintercalation of Al^{3+}): $\quad Al_xC_{3y} - 3e^- \longrightarrow xAl^{3+}{}_{(aq)} + 3C_y$

Reduction (deposition of Zn): $\quad Zn^{2+}{}_{(aq)} + 2e^- \longrightarrow Zn_{(s)}$

During negative potential sweep of CV using C_{3y} (GPGE) as WE (discharging process):

Reduction (intercalation of Al^{3+}): $xAl^{3+}{}_{(aq)} + 3C_y + 3e^- \longrightarrow Al_xC_{3y}$

Oxidation (dissolution of Zn): $Zn_{(s)} - 2e^- \longrightarrow Zn^{2+}{}_{(aq)}$
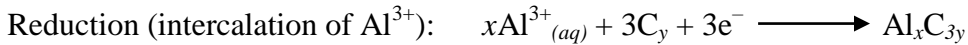
As the results in Figure 4.10 show the potential difference between Zn and GPGE is near about 1.0 V, hence they can be assembled into a rechargeable battery.

The importance of Zn^{2+} ion's presence and also the role of Al^{3+} and Cl^- ions in this electrochemical energy storage system are investigated for the Zn/Al-ion cell by performing CV in aqueous solution of only $AlCl_3$ using Zn and GPGE as negative electrode (CE) and positive electrode (WE), respectively.
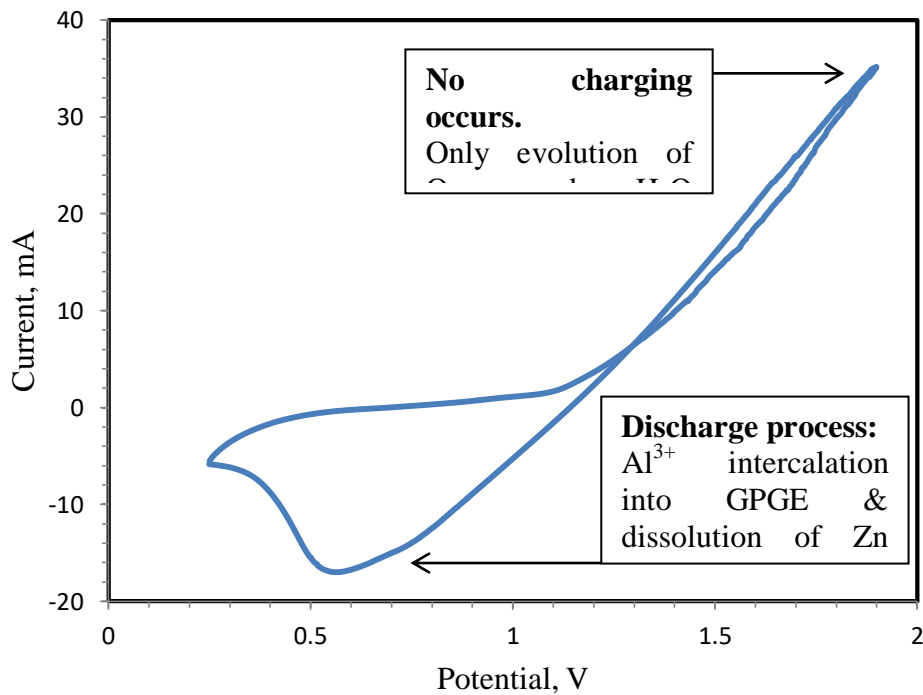
Figure 4.11: CV of Zn/Al-ion cell with GPGE as positive electrode in 0.5M

Reactions:

During negative potential sweep of CV using C_{3y} (GPGE) as WE (discharging process):
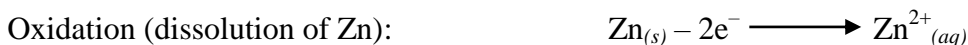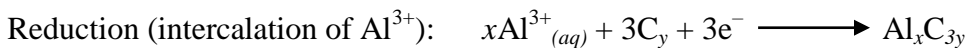
Reduction (intercalation of Al^{3+}): $xAl^{3+}{}_{(aq)} + 3C_y + 3e^- \longrightarrow Al_xC_{3y}$

Oxidation (dissolution of Zn): $Zn_{(s)} - 2e^- \longrightarrow Zn^{2+}{}_{(aq)}$

During positive potential sweep of CV using C_{3y} (GPGE) as WE (charging process):

Oxidation (deintercalation of Al^{3+}): $Al_xC_{3y} - 3e^- \longrightarrow xAl^{3+}{}_{(aq)} + 3C_y$

Reduction (deposition of Al): $Al^{3+}{}_{(aq)} + 3e^- \longrightarrow$ No reduction occurs in aq. medium.
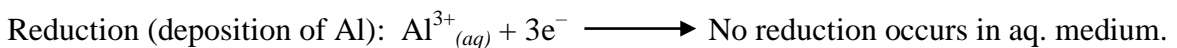
The CV (Figure 4.11) shows that the cell can only be discharged as only a reduction peak is found here. The increase in positive current near about +1.9 V is mainly due to splitting of H_2O into H^+ and OH^- ultimately resulting in evolution of O_2 gas. The absence of oxidation peaks for GPGE as WE verifies that the CE (Zn) is unable to support the redox reaction though reduction of the only available reducible ions (Al^{3+}) from the solution. This can be attributed to very low over-potential for hydrogen evolution of Aluminum which makes the reduction of Al^{3+} ion in aqueous solution to be incompatible. As a result, the use of only $AlCl_3$ as cell electrolyte makes the assembled Zn/Al-ion cell a non-rechargeable one. Hence, to make the Zn/Al-ion cell rechargeable, the presence of metal ions reducible from aqueous medium (here Zn^{2+} ions with high over-potential for H_2 evolution) is also obligatory as electrolyte along with Al^{3+} ions (intercalable into cathodic materials). This process can be supported by the results from CV of Zn (WE) in an $AlCl_3/Zn(CH_3COO)_2$ (0.5/0.5 M) electrolyte at 1 mV/s (Figure 4.12).
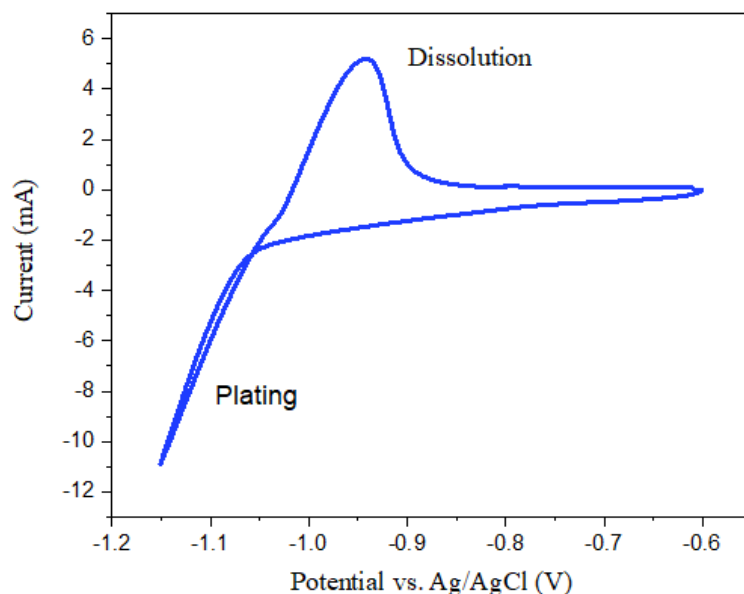
Figure 4.12: CV of Zn in an $AlCl_3/Zn(CH_3COO)_2$ (0.5/0.5 M) electrolyte at 1 mV/s.

As shown in Figure 4.12, the polished zinc electrode has good reversibility in this aqueous electrolyte. It loses electrons (oxidation) and liberates Zn^{2+} at −1.07 V (versus Ag/AgCl) during the discharge process. Then it gains electrons, and zinc is deposited at −0.93 V (versus Ag/AgCl), during the charge process.

Electrochemical performances of aqueous rechargeable Zn/Al-ion battery are shown in Figures (4.13 – 4.22).
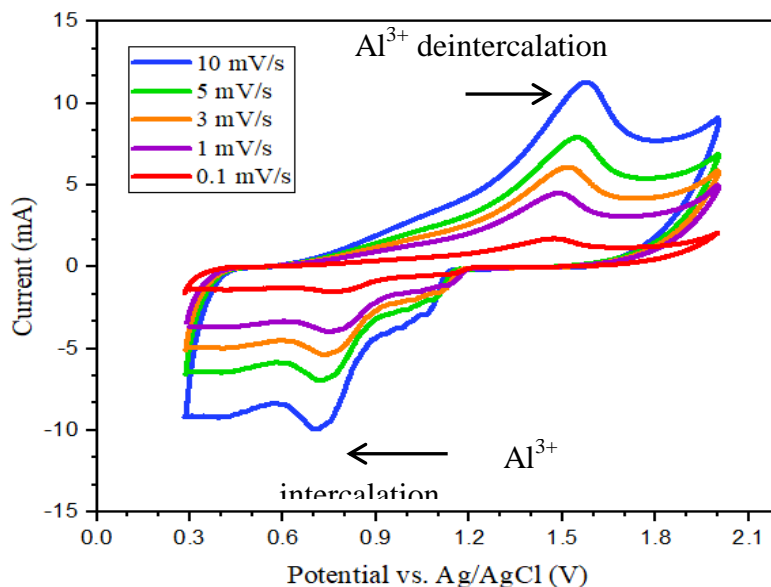
Figure 4.13: CV curves of Zn/Al-ion cell with GPGE positive electrode at different scan rates.
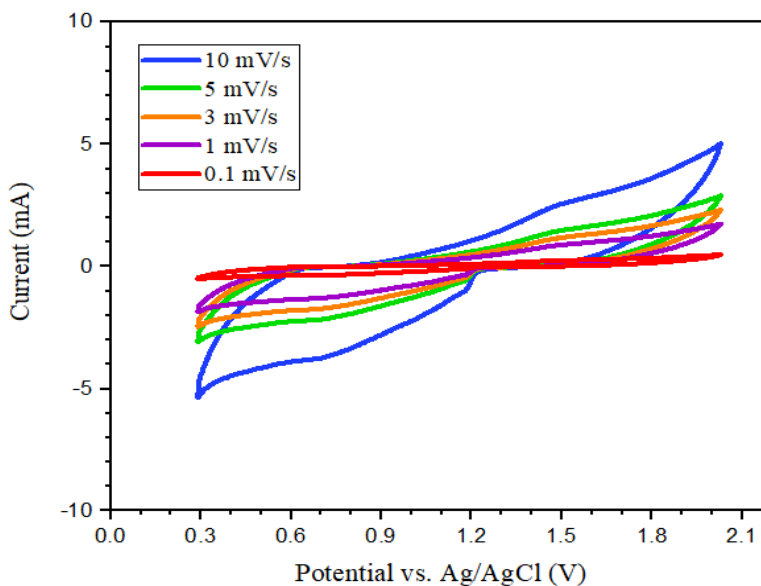
Figure 4.14: CV curves of Zn/Al-ion cell with PGE positive electrode at different scan rates.

Oxidation peak at 1.61 V and reduction peaks at 0.71/1.1 V (Figure 4.14) can be found for a reversible redox reaction from CV of Zn/Al-ion cell with GPGE as positive electrode at a

scan rate of 1 mV s^{-1}. When the scan rate increases, the peak separation becomes larger as a result of the increased over potentials. However, the sharp redox peaks are maintained at the high scan rate (10 mVs^{-1}) indicating high rate capability. In contrast, the oxidation peak of Zn/Al-ion cell with PGE as positive electrode is incomplete with no recognizable oxidation reduction peak (Figure 4.14).

4.4.2 Galvanostatic Charge-discharge Profile of Zn/Al-ion Cell

Specific capacity of the fabricated Zn/Al-ion battery with GPGE as positive electrode is determined (Figure 4.15) to be 56.5 mAhg^{-1} at 1C (55 mA g^{-1}).
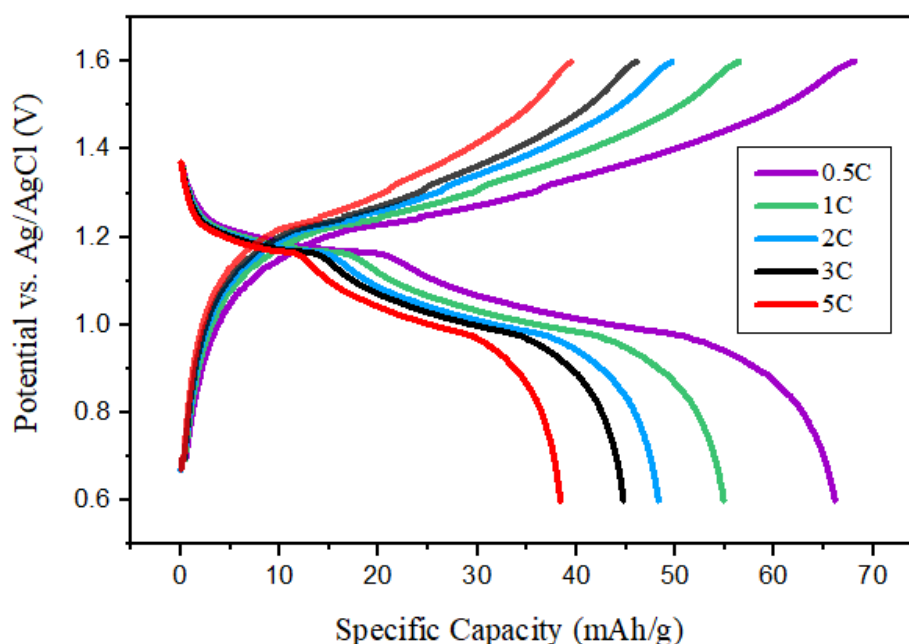
Figure 4.15: Charge/discharge profiles of Zn/Al-ion cell at different C-rates.

A maximum discharge capacity of 66.13 mAhg^{-1} for the GPGE is obtained at 0.5 C-rate with an average discharge voltage of 1.0 V. At 5C, Zn/Al ion cell with GPGE positive electrode shows a discharge capacity of 38.4 mAh g^{-1}.

4.4.3 Chronopotentiometric Study for Cyclic Stability of Zn/Al-ion Cell
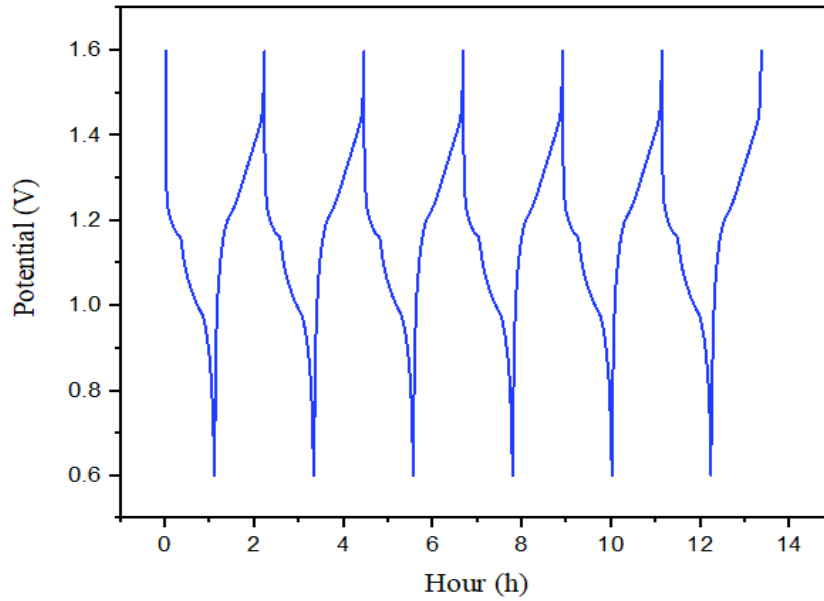
Figure 4.16: Chronopotentiometry of Zn/Al-ion battery for 95th to 100th cycles.

The chronopotentiometry (Figure 4.16) of Zn/Al-ion cell exhibits excellent cyclic stability up to 100 cycles providing a capacity of 54.1 mAhg^{-1} with capacity retention of ~95.8% (Figure 4.17) at 1C (55 mAg^{-1}). The charging time for this Zn/Al-ion cell is also low-enough (~2 hours) which is of great proficiency for large–scale stationary energy storage.

4.4.4 Coulombic Efficiency Study of Zn/Al-ion Cell
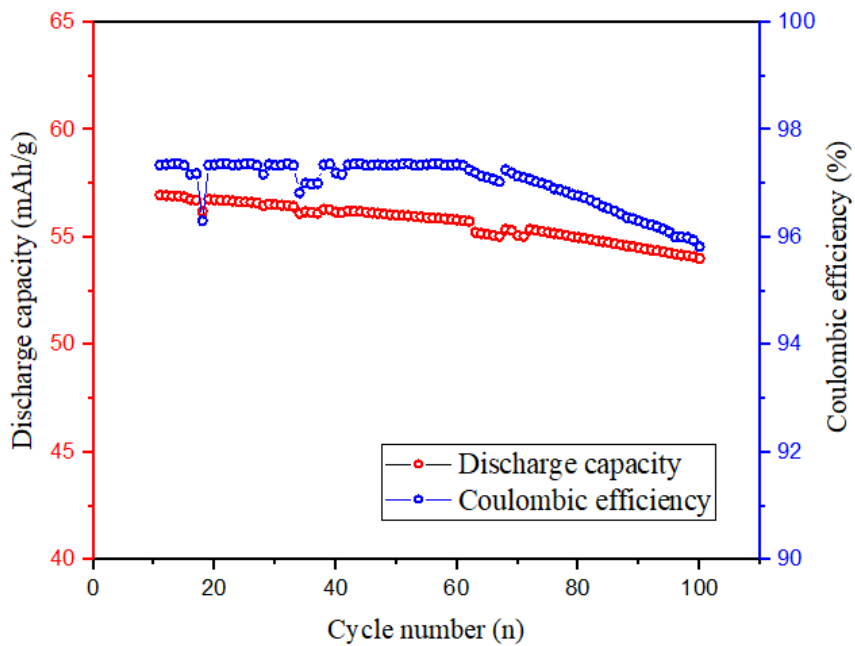
Figure 4.17: Cycling behavior of Zn/Al-ion cell with GPGE as positive electrode.
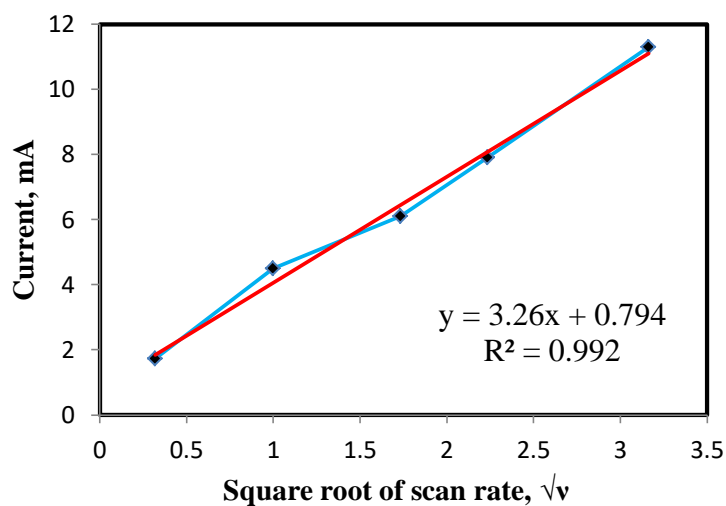
Figure 4.18: The anodic peak current as function of square root of scan rate for Zn/Al-ion cell with GPGE as positive electrode.
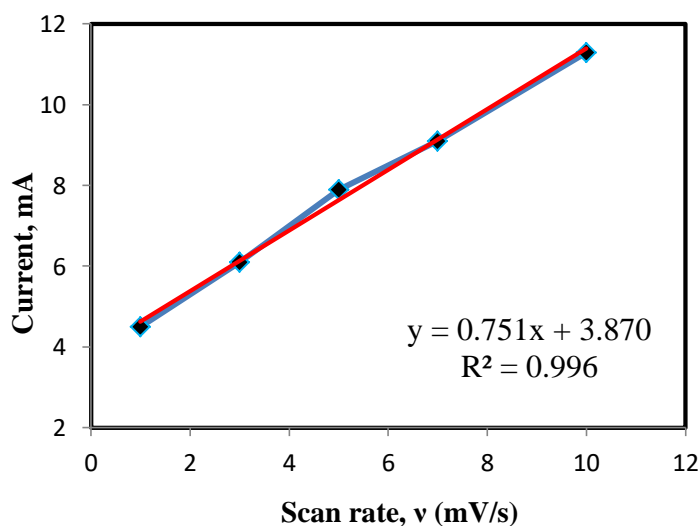
Figure 4.19: The anodic peak current as function of scan rate for Zn/Al-ion cell with GPGE as positive electrode.

From CV curves (Figure 4.13) of Zn/Al-ion cell with GPGE at different scan rates, plots of anodic peak current as function of square root of scan rate (diffusion dependency) and as function of scan rate only (surface area dependency) are presented by correlating with Figure 4.18 and 4.19, respectively. For scan rates ranging from 1 to 10 mV s^{-1}, the R-squared values for anodic peaks are about 0.992 and 0.996, indicating that the kinetics of Zn/Al-ion cell using GPGE as positive electrode in an AlCl$_3$/Zn(CH$_3$COO)$_2$ (0.5/0.5 M) electrolyte interplay between diffusion and surface controlled reactions but more close to a surface–controlled diffusion.

4.4.5 Electrochemical Impedance Spectroscopy (EIS) Analysis of Zn/Al-ion Cell

EIS curves for GPGE and PGE as Zn/Al-ion battery electrode at zero/open circuit potential (OCP) are shown respectively in Figure 4.20 and 4.21.
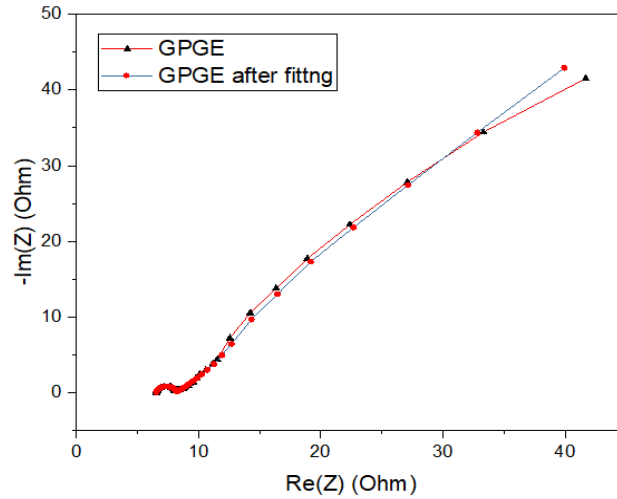
Figure 4.20: Nyquist plot of EIS for Zn/Al-ion cell with GPGE as positive electrode at OCP.
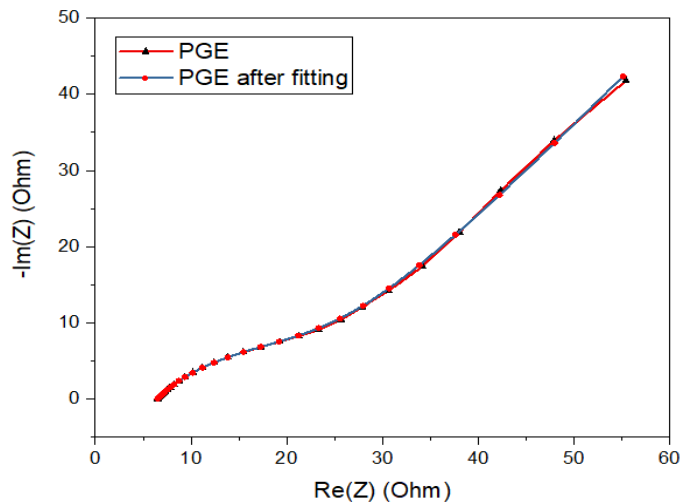
Figure 4.21: Nyquist plot of EIS for Zn/Al-ion cell with PGE as positive electrode at OCP.

Due to the same aqueous electrolyte, the solution resistances (R_s) (from the intercept in the real axis) are the same (6.5 Ω) for both PGE and GPGE. However, the charge–transfer resistance (R_{ct}) is determined to be 8.27 Ω for the GPGE (Figure 4.20), which is evidently lower than 33 Ω for PGE (Figure 4.21), signifying that the GPGE can offer high rate capability. At low frequencies, the linear region with an angle of about 48° suggests that the electrode process is under both diffusion control and surface area dependent. This

electrode behavior is similar to the pseudo capacitive process. This result is consistent with that in Figure 4.18 and 4.19. It is also the reason that the capacity for the GPGE is higher than that of raw PGE.

Electrochemical impedance spectroscopy (EIS) curves are shown for GPGE as Zn/Al-ion battery electrode at charged state (up to 1.6 V) and discharged state (to 0.6 V) in Figure 4.22 and 4.23, respectively.
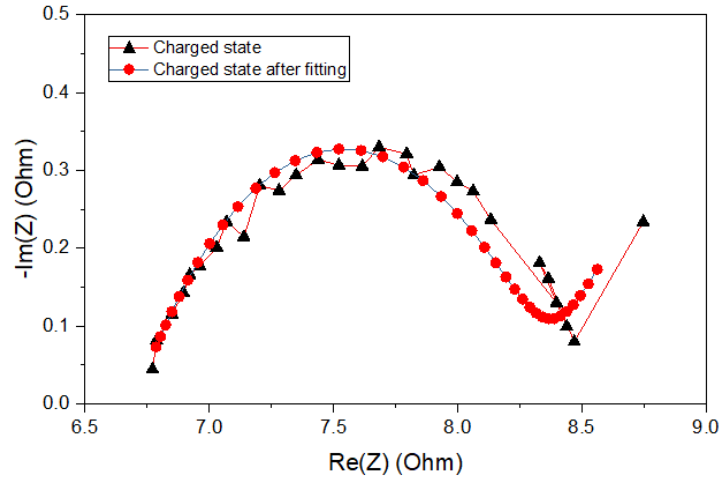
Figure 4.22: Nyquist plot of EIS for Zn/Al ion battery at charged state.

At charged state, the reaction equilibrium rests as follow:

$$3Zn^{2+}_{(aq)} + 2Al_xC_{3y} \longrightarrow 3Zn_{(s)} + 2xAl^{3+}_{(aq)} + 6C_y$$
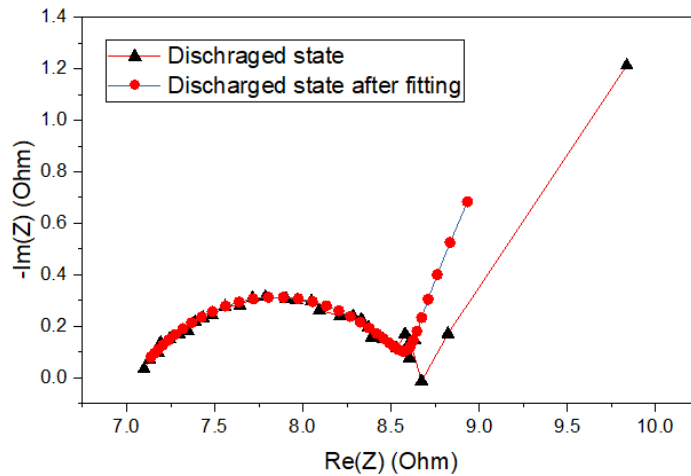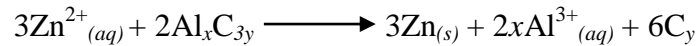
Figure 4.23: Nyquist plot of EIS for Zn/Al ion battery at discharged state.

At discharged state, the reaction equilibrium rests as follow:

$$3Zn_{(s)} + 2xAl^{3+}_{(aq)} + 6C_y \longrightarrow 3Zn^{2+}_{(aq)} + 2Al_xC_{3y}$$
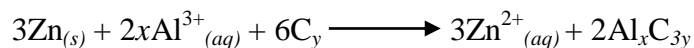
As shown in Figure 4.22, at charged state solution resistance (R_s) value (6.76 Ω) is less than that of discharged state (7.1 Ω) in Figure 4.23. This can be attributed to the presence of more aluminum ions in saturated $Zn(CH_3COO)_2$ solution in charged state as Al^{3+} ion has smaller (ionic radius 67.5 picometer) which is easily movable than Zn^{2+} ion (ionic radius 88 picometer).[108] Charge transfer resistance (R_{ct}) value (8.4 Ω) is also less in charged state due presence of Al-ion's three electrode redox property. In discharged state, Zn metal dissolution causes more Zn^{2+} ion production which combines with relatively more basic CH_3COO^- ions, hence giving rise to more R_s (7.1 Ω) and R_{ct} (8.75 Ω). Due to more internal resistance in discharged state the battery system provides less potential (V) difference between electrodes.

These results indicates the intercalation/deintercalation of smaller Al^{3+} {or $[Al(H_2O)_6]^{3+}$} ions into graphene layers of the GPGE more evidently.
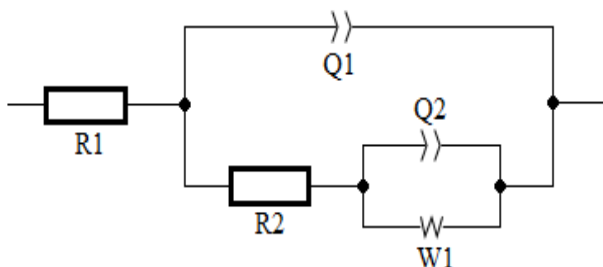
Figure 4.24: Equivalent circuit used for fitting impedance (EIS) spectra.

To obtain a good fit with experimental data, a purely capacitive element (C_d) is substituted with a constant phase element (Q) in the equivalent circuit (Figure 4.24). Here, R_1, R_2 and W_1 are Solution resistance, Charge transfer resistance and Warburg impedance for diffusion controlled process, respectively.

4.5 Characterization of GPGE at Charged and Discharged State by SEM Analysis

Before discharging of Zn/Al-ion cell in aqueous $AlCl_3$/$Zn(CH_3COO)_2$ (0.5/0.5 M) electrolyte., ultrathin sheet like morphology was observed which may due to the presence of two dimensional sp^2 carbon layers of PGE surface (Figure 4.25 a and b).
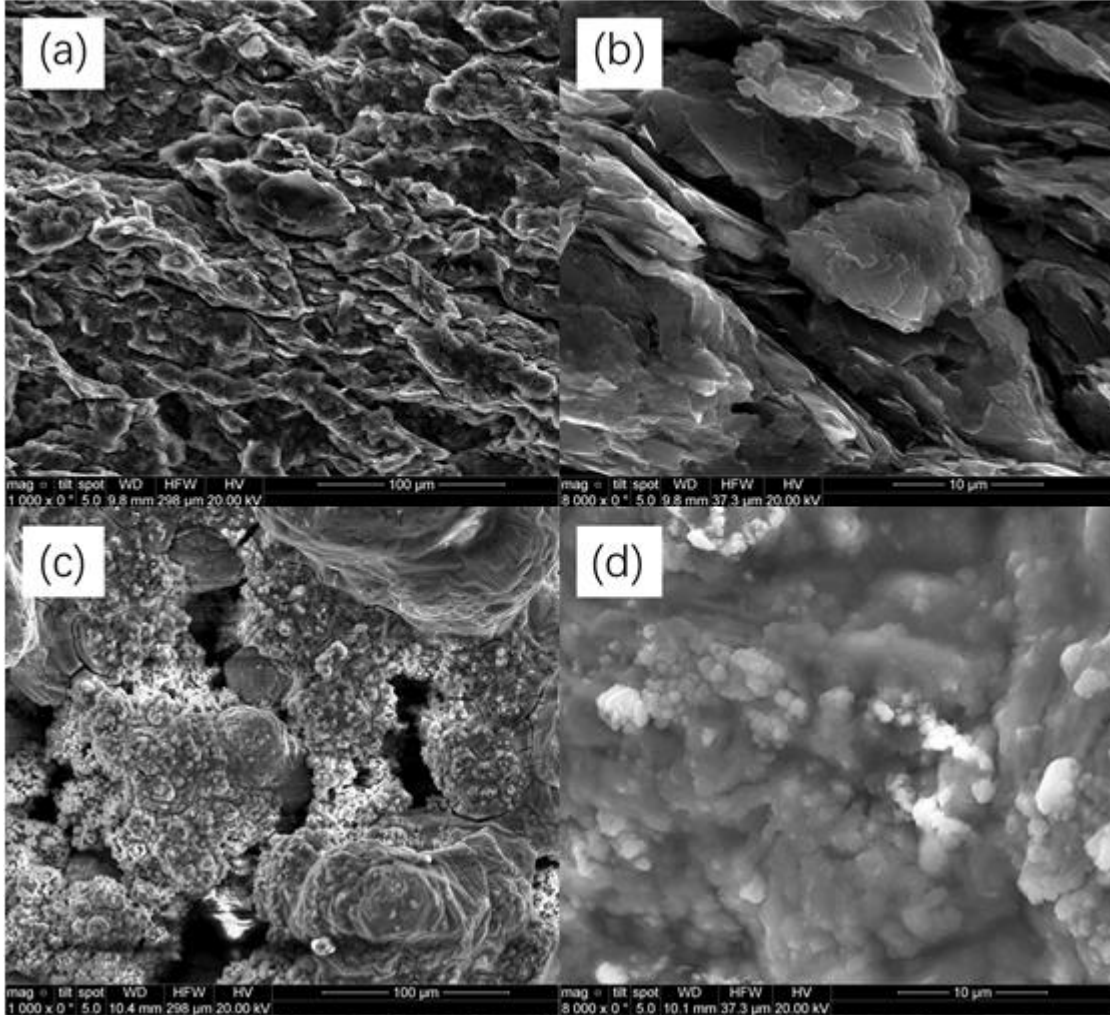
Figure 4.25: SEM images of GPGE before (a-b) and after (c-d) discharging to -0.4V (vs. Ag/AgCl)

After discharging to –0.4V (vs. Ag/AgCl) in a three-electrode system in aqueous $AlCl_3$/$Zn(CH_3COO)_2$ (0.5/0.5 M) electrolyte, granular morphology was obtained (Figure 4.25 c and d). These results indicate the intercalation and/or deposition of Al/Zn into/on cathode (GPGE) accompanied by reduction on the electrode surface with following reaction:

$$Zn^{2+} + 2xAl^{3+}{}_{(aq)} + 6\ C_y + 12x\ e^- \longrightarrow Zn_{(s)} + 2Al_xC_{3y}$$
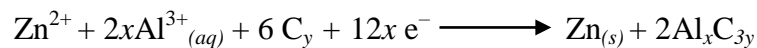
4.6 Characterization of GPGE at Charged and Discharged State by EDX Analysis
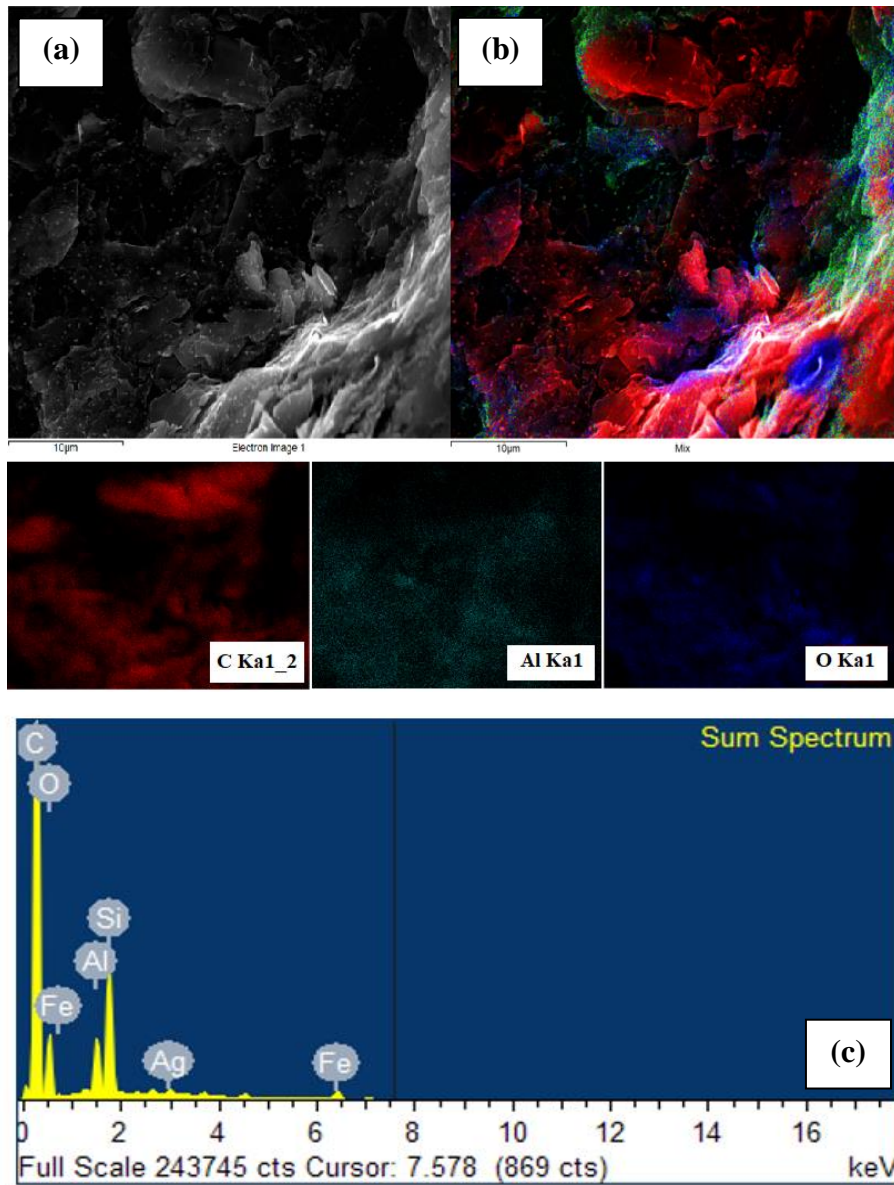
Figure 4.26: SEM (a) and EDX (b) elemental mapping of GPGE before discharging during cycling in a three-electrode system.

Table 4.2: Elemental contents (%) according to EDX spectroscopy before cell discharging.

Elements	Weight percentage (%)	Atomic percentage (%)
Carbon (C)	70.35	78.38
Oxygen (O)	22.08	18.47
Aluminum (Al)	**1.66**	**0.82**
Silicon (Si),	4.14	1.97
Iron (Fe)	1.19	0.28
Silver (Ag)	0.59	0.07
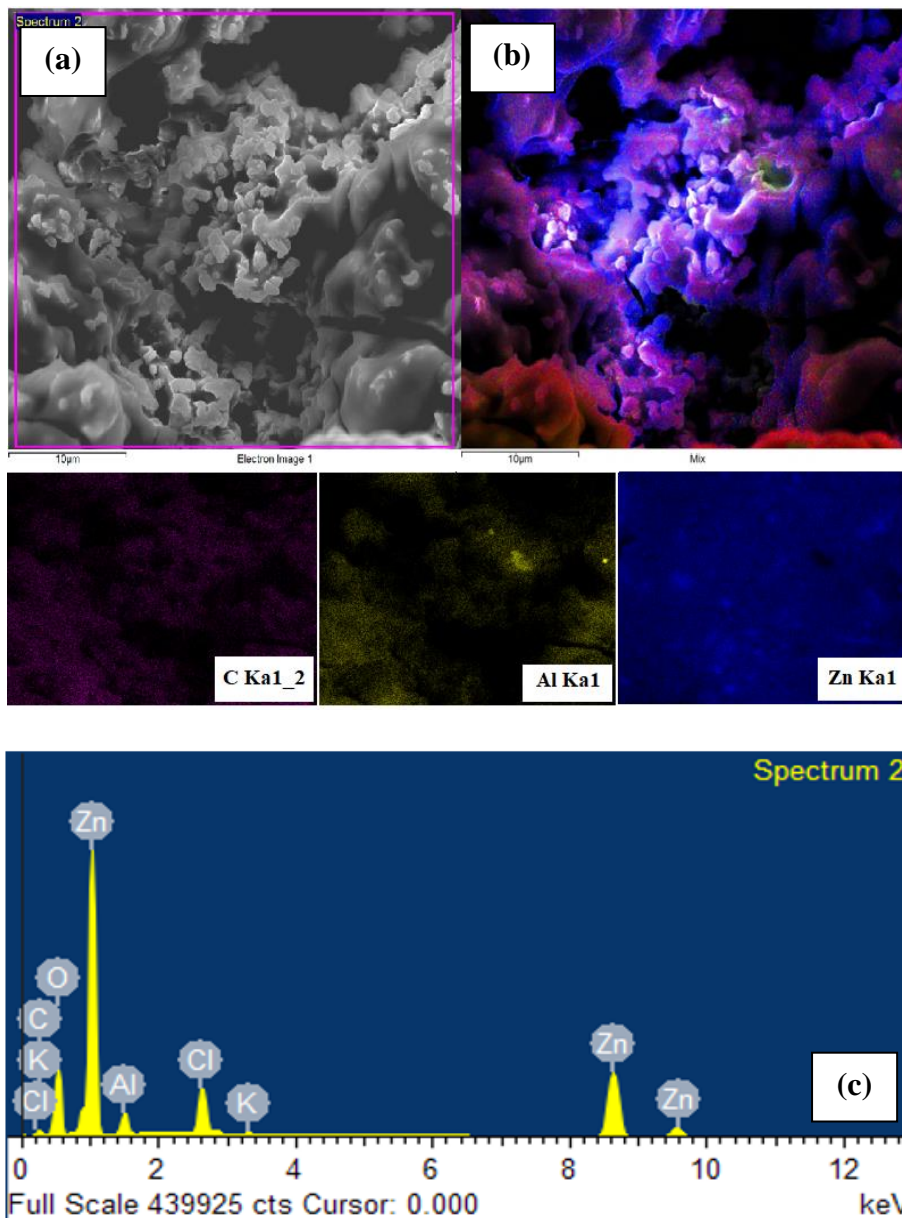
Figure 4.27: SEM (a) and EDX (b) elemental mapping of GPGE after discharging to -0.4V (vs. Ag/AgCl) during cycling in a three-electrode system.

Table 4.3: Elemental contents (%) according to EDX spectroscopy after cell discharging.

Elements	Weight percentage (%)	Atomic percentage (%)
Carbon (C)	4.62	12.33
Oxygen (O)	23.53	47.13
Aluminum (Al)	**3.71**	**4.41**
Chlorine (Cl)	6.53	5.91
Potassium (K)	0.08	0.07
Zinc (Zn)	**61.52**	**30.16**

Energy Dispersive X-ray spectroscopy (EDX) of GPGE surfaces before and after discharging the fabricated Zn/Al-ion cell are shown in Figure 4.26(b) and 4.27(b) respectively. EDX analysis shows that the Al contents (atomic percentage) had been increased from 0.82% to 4.41% after deep discharging to −0.4 Volt. This represents the accumulation or intercalation of Aluminum in GPGE cathode undergoing through reduction reaction. It was also observed that the Zinc was almost absent before discharging (Figure 4.26 c), rather due to deep discharging to −0.4V, the atomic percentage of Zn content was highly increased to 30.16% (Figure 4.27 c). This result signifies that Zinc was deposited on the outer surface of GPGE only when discharged deeply, where Al-ion can undergo intercalation into inner layer of GPGE due to its smaller ionic radius.

The chemical reactions reversibility involves two types of chemistry upon cycling, which are dissolution/deposition of Zinc (Zn/Zn^{2+}) and surface redox process of Al-ion intercalation/ deintercalation involving graphene layers on pencil graphite electrode (GPGE), as shown in Scheme 4.
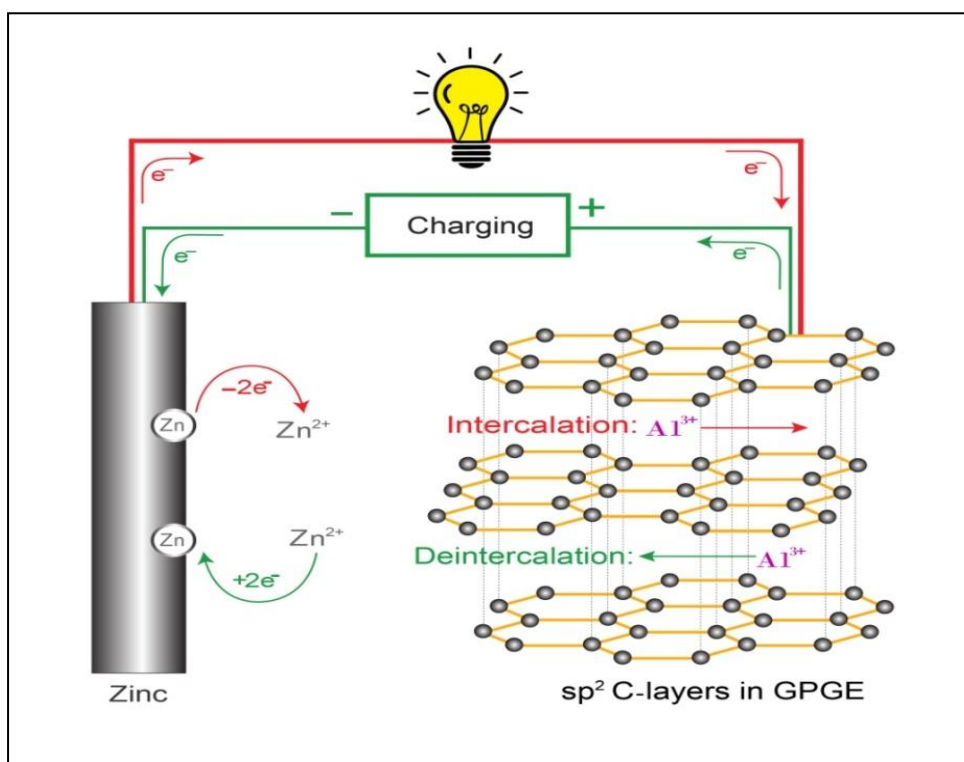
Scheme 4: Schematic illustration of redox reactions for an aqueous rechargeable battery during the charge and discharge process comprised of a zinc metal anode vs. graphene coated pencil graphite (GPGE) as cathode. Charging is indicated by green arrows and discharging is indicated by red arrows for the electrons and the ions transfer.

During discharging process:

Oxidation: $3Zn_{(s)} - 6e^- \longrightarrow 3Zn^{2+}_{(aq)}$

Reduction: $2xAl^{3+}_{(aq)} + 6C_y + 6e^- \longrightarrow 2Al_xC_{3y}$

Total reaction: $3Zn_{(s)} + 2xAl^{3+}_{(aq)} + 6C_y \longrightarrow 3Zn^{2+}_{(aq)} + 2Al_xC_{3y}$
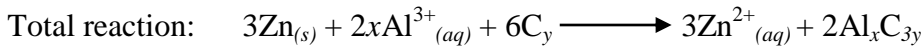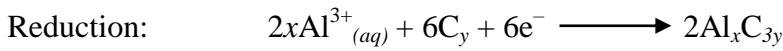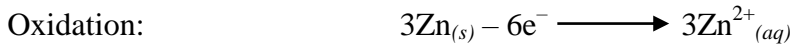
During charging process:

Oxidation: $3Zn^{2+}_{(aq)} + 6e^- \longrightarrow 3Zn_{(s)}$

Reduction: $2Al_xC_{3y} - 6e^- \longrightarrow 2xAl^{3+}_{(aq)} + 6C_y$

Total reaction: $3Zn^{2+}_{(aq)} + 2Al_xC_{3y} \longrightarrow 3Zn_{(s)} + 2xAl^{3+}_{(aq)} + 6C_y$
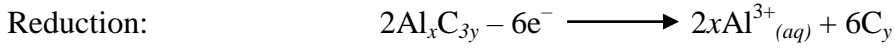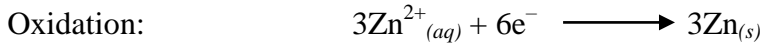
The moderate capacity, high rate capability and cycling stability of this aqueous rechargeable Al-ion battery can be credited to the exclusive graphene's ultrathin nano structure on the pencil graphite. The thin graphene structure is readily accessible for the electrolyte, facilitating the transportation of Al^{3+} ions from liquid to the active surface of GPGEs. Meanwhile, the enlarged specific surface area may provide a larger space for Al^{3+} ion intercalation into the outer graphene layers of GPGEs. Previously, MoS_2 and V_2O_5 with a larger surface area and inter layer distance significantly enhance the reversible ion insertion−extraction kinetics for various batteries (Li ion battery [112], Na ion battery [113], and Mg ion battery [114] etc.). In this system, the average charge and discharge voltages are 1.2 and 1.0 V, respectively, which is competitive with aqueous Al-ion battery using Ultrathin Graphitic nano-sheet [53] but can exceed those of the recently reported $Al//V_2O_5$ (average charge and discharge voltages are 0.8 and 0.6 V) [7, 8] and $Al//VO_2$ (average charge and discharge voltages are 0.7 and 0.5 V) [6] in an ionic liquid electrolyte. Although, its specific capacity (56.46 mAh g^{-1}) is lower than those of using ionic liquid electrolyte, still considering cost and ease of fabrication, it is more competent when compared to pyrolytic graphite in $AlCl_3$/EMIC electrolyte (<70 mA.h.g^{-1}) [9] and the chloride ion battery in ionic liquid electrolyte [115], TiO_2 nanotubes [52] and prussian blue analogue nanoparticles [43, 51] in $AlCl_3$ and $Al(NO_3)_3$ aqueous electrolytes.

The cycling behavior is also excellent (95.8% up to 100 cycles) as compared to most of the Al ion batteries in ionic liquid and aqueous electrolyte [5−8, 10, 52]. Moreover, the positive electrode (GPGE) preparation method is easier to than the oxidation method for chemically modified graphene nanosheets [116, 117]. Most importantly, the cost of our used electrolyte is lower than that of an ionic liquid electrolyte. In case of the negative electrode, zinc is also a low–cost and nontoxic material produced on a large scale of

approximately 12million tons per year [33]. The dendrite formation is normally a limitation against rechargeable zinc electrodes which have not been observed in this system within 100 cycles. Before the practical application of this aqueous rechargeable Zn/Al ion battery, another problem on this kind of battery system is that it needs to use a highly concentrated Al salt electrolyte to obtain high energy density, similar to dual–graphite cells [118]. Zinc electrode may undergo corrosion due to highly acidic nature of the electrolyte made from concentrated Aluminum salt.

CHAPTER V

Conclusions and Recommendations

In conclusion, a new aqueous rechargeable Zn/Al-ion battery has been developed which uses graphene coated pencil graphite (GPGE) as the positive electrode and zinc metal as the negative electrode in a mixed electrolyte of aqueous 0.5 M $AlCl_3$ and 0.5 M $Zn(CH_3COO)_2$. A facile electrochemically expanded cyclic voltametric method was used to prepare the graphene layers on pencil graphite surface. The larger specific surface area of this ultrathin graphene layer provides a larger space for Al-ion intercalation into the outer graphene layers as well as for deposition of Zn at outer surface of the pencil graphite. Thus, this rechargeable battery can offer good capacity while maintaining a moderate current density during charging and discharging. When compared to most rechargeable aluminum ion batteries in ionic liquid electrolytes, it can provide a good working voltage (average 1.0 V) and efficient cycling performances (over 100 charging/ discharging cycles) with very low cost and easy assembling method. These results reveal the possibility for potential application of aqueous rechargeable Zn/Al-ion batteries in immobile energy storage technology.

Recommendations

In present work, no Zinc dendrite was formed on the anode within 100 cycles, which is very likely to occur when more cycling is performed as it is a common limitation for rechargeable zinc battery. Slight volume expansion of GPGE was also observed during cycling which may cause cathode disintegration limiting the cycle life. Moreover, highly acidic of $AlCl_3$-electrolyte is prone to corrode the Zinc metal which may give rise to self-discharging and capacity loss. To overcome these inherent problems following recommendations can be proposed:

➢ Pro-active designing of anodic materials (like using hyper dendritic nano-porous 3D-zinc foam as anode).

➢ Utilizing 3D- Nickel foam surface supported graphene layers as cathodic material.

➢ Investigating for Al-salt solution or electrolyte made of Al-salt mixed with other salt offering lower acidity and improved electrochemical activity.

REFERENCES

1. Winter, M. and Brodd, R. J., 2004, "What are Batteries, Fuel cells, and Supercapacitors?" Chem. Rev., Vol. 104, pp. 4245−4269.

2. Dunn, B., Kamath, H. and Tarascon, J. M., 2011, "Electrical Energy Storage for the Grid: A Battery of Choices." Science, Vol. 334, pp. 928−935.

3. Das, S. K., Mahapatra, S. and Lahan, H., 2017, "Aluminium−ion batteries: developments and Challenges." J. Mater. Chem. A, Vol. 5, pp. 6347−6367.

4. Larcher, D. and Tarascon, J. M., 2015, "Towards Greener and More Sustainable Batteries for Electrical Energy Storage." Nat. Chem., Vol. 7, pp. 19−29.

5. Hudak, N. S., 2014, "Chloroaluminate−Doped Conducting Polymers as Positive Electrodes in Rechargeable Aluminum Batteries." J. Phys. Chem., Vol. C118, pp. 5203−5215.

6. Wang, W., Jiang, B., Xiong, W., Sun, H., Lin, Z., Hu, L., Tu, J., Hou, J., Zhu, H. and Jiao, S., 2013, "A New Cathode Material for Super−Valent Battery Based on Aluminium Ion Intercalation and Deintercalation." Sci. Rep., Vol. 3, pp. 3383−3388.

7. Jayaprakash, N., Das, S. K. and Archer, L. A., 2011, "The Rechargeable Aluminum−Ion Battery." Chem. Commun., Vol. 47, pp. 12610−12612.

8. Reed, L. D. and Menke, E., 2013, "The Roles of V_2O_5 and Stainless Steel in
a. Rechargeable Al−Ion Batteries." J. Electrochem. Soc., Vol. 160, pp. A915−A917.

9. Lin, M. C., Gong, M., Lu, B., Wu, Y., Wang, D. Y., Guan, M., Angell, M., Chen, C., Yang, J., Hwang, B. J. and Dai, H., 2015, "An Ultrafast Rechargeable Aluminium−Ion Battery." Nature, Vol. 520, pp. 324−328.

10. Rani, J. V., Kanakaiah, V., Dadmal, T., Rao, M. S. and Bhavanarushi, S., 2013, "Fluorinated Natural Graphite Cathode for Rechargeable Ionic Liquid based Aluminum−Ion Battery." J. Electrochem. Soc., Vol. 160, pp. A1781−A1784.

11. Tang, W., Hou, Y. Y., Wang, F. X., Liu, L. L., Wu, Y. P. and Zhu, K., 2013, "$LiMn_2O_4$ Nanotube as Cathode Material of Second−level Charge Capability for Aqueous Rechargeable Batteries." Nano Lett., Vol. 13, pp. 2036−2040.

12. Pasta, M., Wessells, C. D., Huggins, R. A. and Cui, Y., 2012, "A High−Rate and Long Cycle Life Aqueous Electrolyte Battery for Grid−Scale Energy Storage." Nat. Commun., Vol. 3, pp. 1149−1155.

13. White, C. D. and Zhang, K. M., 2011, "Using Vehicle−to−Grid Technology for Frequency Regulations and Peak−load Reduction." J. Power Sources, Vol. 196, pp. 3972−3980.

14. Pasta, M., Wessells, C. D., Huggins, R. A. and Cui, Y., 2012, "A High−Rate and Long Cycle Life Aqueous Electrolyte Battery for Grid−Scale Energy Storage." Nat. Commun., Vol. 3, pp. 1149−1155.

15. Wang, H. L., Liang, Y. Y., Gong, M., Li, Y. G., Chang, W., Mefford, T., Zhou, J. G., Wang, J., Regier, T., Wei, F. and Dai, H. J., 2012, "An Ultrafast Nickel−Iron Battery from Strongly Coupled Inorganic Nanoparticle/nanocarbon Hybrid Materials." Nat. Commun. Vol. 3, pp. 917−924.

16. Kundu, D., Adams, B. D., Duffort, V., Vajargah, S. H. and Nazar L. F., 2016, "A high−capacity   and long−life aqueous rechargeable zinc battery using a metal oxide intercalation cathode." Nature Energy, Vol. 1, pp. 1−8.

17. Xu, C., Li, B., Du, H. and Kang, F., 2012, "Energetic Zinc Ion Chemistry: The Rechargeable Zinc Ion Battery." Angew. Chem. Int. Ed., Vol. 51, pp. 933−935.

18. Zhang, L., Chen, L., Zhou, X. and Liu, Z., 2015, "Towards High−Voltage Aqueous Metal−Ion Batteries Beyond 1.5 V: The Zinc/Zinc Hexacyanoferrate System." Adv. Energy Mater., Vol.5, pp. 1400930−1400931.

19. Gong, M., Li, Y., Zhang, H., Zhang, B., Zhou, W., Feng, J., Wang, H., Liang, Y., Fan, Z., Liu, J. and Dai, H., 2014, "Ultrafast High−Capacity Ni//Zn Battery with NiAlCo−Layered Double Hydroxide." Energy Environ. Sci., Vol. 7, pp. 2025−2032.

20. Wang, X., Li, M., Wang, Y., Chen, B., Zhu, Y. and Wu, Y., 2015, "A Zn−NiO Rechargeable Battery with Long Lifespan and High EnergyDensity." J. Mater. Chem. A., Vol. 3, pp. 8280−8283.

21. Zhang, B. H., Liu, Y., Wu, X. W., Yang, Y. Q., Chang, Z., Wen, Z. B. and Wu, Y. P., 2014, "An Aqueous Rechargeable Battery Based on Zinc Anode and $Na_{0.95}MnO_2$." Chem. Commun., Vol. 50, pp. 1209−1211.

22. Li, Z., Young, D., Xiang, K., Carter, W. C. and Chiang, Y. M., 2013, "Towards High Power High Energy Aqueous Sodium−Ion Batteries: The $NaTi_2(PO_4)_3/Na_{0.44}MnO_2$ System. Adv. Energy Mater. Vol. 3, pp. 290−294.

23. Liu, Y., Zhang, B. H., Xiao, S. Y., Liu, L. L., Wen, Z. B. and Wu, Y. P., 2014, "A Nanocomposite of MoO_3 Coated with PPy as an Anode Material for Aqueous Sodium Rechargeable Batteries with Excellent Electrochemical Performance." Electrochim. Acta, Vol. 116, pp. 512−517.

24. Li, W., Dahn, J. R. and Wainwright, D. S., 1994, "Rechargeable Lithium Battery with Aqueous Electrolytes." Science, Vol. 264, pp. 1115−1118.

25. Wang, G. J., Fu, L. J., Zhao, N. H., Yang, L. C., Wu, Y. P. and Wu, H. Q., 2007, "An Aqueous Rechargeable Lithium Battery with Good Cycling Performance." Angew. Chem., Int. Ed., Vol. 46, pp. 295−297.

26. Wang, F. X., Xiao, S. Y., Shi, Y., Liu, L. L., Zhu, Y. S., Wu, Y. P., Wang, J. Z. and Holze, R., 2013, "Spinel $LiNi_xMn_{2-x}O_4$ as Cathode Material for Aqueous Rechargeable Lithium Batteries." Electrochim. Acta Vol. 93, pp. 301−306.

27. Tang, W., Zhu, Y., Hou, Y., Liu, L., Wu, Y., Loh, K. P., Zhang, H. and Zhu, K. 2013, "Aqueous Rechargeable Lithium Batteries as an Energy Storage System of Superfast Charging." Energy Environ. Sci., Vol. 6, pp. 2093−2104.

28. Kim, H., Hong, J., Park, K. Y., Kim, H., Kim, S. W. and Kang, K., 2014, "Aqueous Rechargeable Li and Na Ion Batteries." Chem. Rev. Vol. 114, pp. 11788−11827.

29. Wang, F. X., Xiao, S. Y., Chang, Z., Yang, Y. Q. and Wu, Y. P., 2013, "Nanoporous $LiNi_{1/3}Co_{1/3}Mn_{1/3}O_2$ as an Ultra−fast Charge Cathode Material for Aqueous Rechargeable Lithium Batteries." Chem. Commun., Vol. 49, pp. 9209−9211.

30. Mahesh, K. C., Suresh, G. S., Bhattacharyya, A. J., Venkatesha, T. V., 2012, "Synthesis and Electrochemical Characterization of $LiNi_{0.8}Co_{0.2}O_2$ as Cathode Material for Aqueous Rechargeable Lithium Batteries." J. Electrochem. Soc., Vol. 159, pp. A571−A578.

31. Tang, W., Hou, Y. Y., Wang, F. X., Liu, L. L., Wu, Y. P. and Zhu, K., 2013, "$LiMn_2O_4$ Nanotube as Cathode Material of Second−level Charge Capability for Aqueous Rechargeable Batteries." Nano Lett., Vol. 13, pp. 2036−2040.

32. Wang, X. J., Qu, Q. T., Hou, Y. Y., Wang, F. X. and Wu, Y. P., 2013, "An Aqueous Rechargeable Lithium Battery of High Energy Density Based on Coated Li Metal and $LiCoO_2$." Chem. Commun., Vol. 49, pp. 6179−6181.

33. Wang, F., Liu, Y., Wang, X., Chang, Z., Wu, Y. and Holze, R., 2015, "Aqueous Rechargeable Battery Based on Zinc and A Composite of $LiNi_{1/3}Co_{1/3}Mn_{1/3}O_2$." Chem. ElectroChem. Vol. 2, pp. 1024−1030.

34. Liu, Y., Wen, Z. B., Wu, X. W., Wang, X. W., Wu, Y. P. and Holze, R., 2014, "An Acid−free Rechargeable Battery Based on $PbSO_4$ and Spinel $LiMn_2O_4$., Chem. Commun., Vol. 50, pp. 13714−13717.

35. Ge, H., Li, N., Li, D., Dai, C. and Wang, D., 2008, "Study on the effect of Li doping in spinel $Li_{4+x}Ti_{5-x}O_{12}$ ($0 \leqslant x \leqslant 0.2$) materials for lithium−ion batteries." Electrochemistry Communication, Vol. 10, pp. 1031−1034.

36. Zheng, L., Young, D., Xiang, K., Carter,W. C. and Chiang, Y. M., 2012, "Towards High Power High Energy Aqueous Sodium−ion Batteries: The $NaTi_2(PO_4)_3$/ $Na_{0.44}MnO_2$ System." Adv. Energy Mater., Vol. 3, pp. 290−294.

37. Pasta, M. et al., 2014, "Full Open−Framework Batteries for Stationary Energy Storage." Nat. Commun. Vol. 5, pp. 3007−3008.

38. Wessells, C. D., Huggins, R. A. and Cui, Y., 2011, "Copper Hexacyanoferrate Battery Electrodes with Long Cycle Life and High Power." Nat. Commun. Vol. 2, pp. 550−551.

39. Wessells, C. D., Peddada, S. V., Huggins, R. A. and Cui, Y., 2011, "Nickel Hexacyanoferrate Nanoparticle Electrodes for Aqueous Sodium and Potassium Ion Batteries." Nano Lett. Vol. 11, pp. 5421−5425.

40. Li, W., Dahn, J. R. and Wainwright, D. S., 1994, "Rechargeable Lithium Batteries with Aqueous Electrolytes." Science, Vol. 264, pp. 1115−1118.

41. Kohler, J., Makihara, H., Uegaito, H., Inoue, H. and Toki, M., 2000, "LiV_3O_8: Characterization as Anode Materials for An Aqueous Rechargeable Li−ion Battery System." Electrochim. Acta Vol. 46, pp. 59−65.

42. Luo, J. Y., Cui,W. J., He, P. and Xia, Y. Y., 2010, "Raising the cycling stability of aqueous lithium ion batteries by eliminating oxygen in the electrolyte." Nat. Chem., Vol. 2, pp. 760−765.

43. Zheng, L., Xiang, K., Xing,W., Carter,W. C. and Chiang, Y. M., 2015, "Reversible Aluminum−ion Intercalation in Prussian Blue Analogs and Demonstration of a High−power Aluminum−ion Asymmetric Capacitor." Adv. Energy Mater., Vol. 5, pp. 1401410−1401415.

44. Xu, C. J., Li, B. H., Du, H. D. and Kang, F. Y., 2012, "Energetic zinc ion chemistry: the rechargeable zinc ion battery." Angew. Chem. Int. Ed., Vol. 51, pp. 933−935.

45. Zhang, L., Chen, L., Zhou, X. and Liu, Z., 2015, "Towards high−voltage aqueous metal−ion batteries beyond 1.5 V: the zinc/zinc hexacyanoferrate system." Adv. Energy Mater., Vol. 5, pp. 1400930−1400931.

46. Alfaruqi, M. H. et al., 2015, "Electrochemically induced structural transformation in a −MnO$_2$ cathode of a high capacity zinc−ion battery system." Chem. Mater., Vol. 27, pp. 3609−3620.

47. Zhang, X. G., 1996, "Corrosion and Electrochemistry of Zinc" Springer.

48. Chamoun, M. & Steingart, D. et al., 2015, "Hyper−dendritic nanoporous zinc foam anodes." NPG Asia Mater., Vol. 7, pp. 178−179.

49. Wang, F., Yu, F., Wang, X., Chang, Z., Fu, L., Zhu, Y., Wen, Z., Wu, Y., and Huang W., 2016, "Aqueous Rechargeable Zinc/Aluminum Ion Battery with Good Cycling Performance." ACS Appl. Mater. Interfaces, Vol. 8, pp. 9022−9029.

50. Liu, S., Hu, J. J., Yan, N. F., Pan, G. L., Li, G. R. and Gao, X. P., 2012, "Aluminum Storage Behavior of Anatase TiO$_2$ Nanotube Arrays in Aqueous Solution for Aluminum Ion Batteries." Energy Environ. Sci., Vol. 5, pp. 9743−9746.

51. Li, Z., Xiang, K., Xing, W., Carter, W. C. and Chiang, Y. M., 2015, "Reversible Aluminum−Ion Intercalation in Prussian Blue Analogs and Demonstration of A High−Power Aluminum−Ion Asymmetric Capacitor." Adv. Energy Mater., Vol. 5, pp. 1401410−1401415.

52. Liu, S., Pan, G. L., Li, G. R. and Gao, X. P., 2015, "Copper Hexacyanoferrate Nanoparticles as Cathode Material for Aqueous Al−Ion Batteries." J. Mater. Chem. A., Vol.3, pp. 959−962.

53. Allen, M. J., Tung, V. C. and Kaner, R.B., 2009, "Honeycomb carbon: a review of graphene." Chem. Rev., Vol. 110, pp. 132−133.

54. Pumera, M., 2010, "Graphene−based nanomaterials and their electrochemistry." Chem. Soc. Rev., Vol. 39, pp. 4146−4147.

55. Novoselov, K. S., Geim, A. K., Morozov, S. V., Jiang, D., Zhang, Y., Dubonos, V. S., Grigorieva, I.V. and Firsov, A. A., 2004, "Electric field effect in atomically thin carbon films." Science, Vol. 306, pp. 666−667.

56. Bolotin, K.I., Sikes, K.J., Jiang, Z., Klima, M., Fudenberg, G., Hone, J., Kim P. and Stormer, H.L., 2008, "Ultrahigh electron mobility in suspended graphene," Solid State Commun., Vol. 146, pp. 351−352.

57. Morozov S.V., Novoselov, K.S., Katsnelson, M.I., Schedin, F., Elias, D.C., Jaszczak, J.A. and Geim, A.K., 2008, "Giant intrinsic carrier mobilities in graphene and its bilayer" Phys. Rev. Lett., Vol. 100, pp. 16602−16603.

58. Li, X., Zhu, Y., Cai, W., Borysiak, M., Han, B., Chen, D., Piner, R.D., Colombo, L. and Ruoff, R.S., 2009, "Transfer of large−area graphene films for high−performance transparent conductive electrodes." Nano Lett., Vol. 9, pp. 4359−4360.

59. Zhu, Y., Murali, S., Cai, W., Li, X., Suk, J.W., Potts, J.R. and Ruoff, R.S., 2010, "Graphene and graphene oxide: synthesis, properties, and applications." Adv. Mater., Vol. 22, pp. 3906−3907.

60. Balandin, A.A., Ghosh, S., Bao, W., Calizo, I., Teweldebrhan, D., Miao F. and Lau, C.N., 2008 "Superior thermal conductivity of single−layer graphene." Nano Lett., Vol. 8, pp. 902−903.

61. Lee, C., Wei, X.D., Kysar, J.W. and Hone, J., 2008, "Measurement of the elastic properties and intrinsic strength of monolayer graphene." Science, Vol.321, pp. 385−386.

62. Brownson, D.A.C., Kampouris, D.K. and Banks, C.E., 2012, "Graphene electrochemistry: fundamental concepts through to prominent applications" Chem. Soc. Rev., Vol. 41, pp. 6944−6945.

63. Cai, W., Zhu, Y., Li, X., Piner, R.D. and Ruoff, R.S., 2009, "Large area few−layer graphene/ graphite films as transparent thin conducting electrodes." Appl. Phys. Lett., Vol. 95, pp. 123115−123116.

64. Pu, N., Shi, G., Liu, Y., Sun, X., Chang, J., Sun, C., Ger, M., Chen, C., Wang, P., Peng, Y., Wu, C. and Lawes, S., 2015, "Graphene grown on stainless steel as a

high−performance and ecofriendly anti−corrosion coating for polymer electrolyte membrane fuel cell bipolar plates." J. Power Sources, Vol. 282, pp. 248−249.

65. Hoa, L.T., Sun, K.G. and Hur, S.H., 2015, "Highly sensitive non−enzymatic glucose sensor based on Pt nanoparticle decorated graphene oxide hydrogel." Sensor Actuator B, Vol. 210 pp. 618−619.

66. Pruna, A., Reyes−Tolosa, M.D., Pullini, D., Hernandez−Fenollosa, M.A. and Busquets−Mataix, D., 2015, "Seed−free electrodeposition of ZnO bi−pods on electrophoretically−reduced graphene oxide for optoelectronic applications." Ceram. Int., Vol. 41 pp. 2381−2382.

67. Gao, H. and Duan, H., 2015, "2D and 3D graphene materials: Preparation and bioelectrochemical applications." Biosens. and Bioelectron., Vol. 65, pp. 404−405.

68. Jin, H., Wang, X., Gu, Z., Fan, Q., and Luo, B., 2015, "A facile method for preparing nitrogendoped graphene and its application in supercapacitors." J. Power Sources, Vol. 273, pp. 1156−1157.

69. Zhang, J., Guo, B., Yang, Y., Shen, W., Wang, Y., Zhou, X., Wu, H. and Guo, S., 2015, "Large scale production of nanoporous graphene sheets and their application in lithium ion battery." Carbon, Vol. 84, pp. 469−470.

70. Wang, H., Feng, H. and Li, J., 2014, "Graphene and graphene−like layered transition metal dichalcogenides in energy conversion and storage." Small Vol. 10, pp. 2165−2166.

71. Shi L., Liu, S., He, Z. and Shen, J., 2014, "Nitrogen−doped graphene: effects of nitrogen species on the properties of the vanadium redox flow battery." Electrochim. Acta., Vol. 138, pp. 93−99.

72. Jin, J., Fu, X., Liu, Q., Liu, Y., Wei, Z., Niu, K. and Zhang, J., 2013, "Identifying the active site in nitrogen−doped graphene for the VO^{2+}/VO_2^+ redox reaction." ACS Nano, Vol. 7, pp. 4764−4770.

73. Bose, S., Kuila, T., Kim, N.H., Lee, J.H., Skákalová, V., Kaiser, A.B., (Eds.), 2014, "Graphene produced by electrochemical exfoliation." Woodhead Publishing Ltd., Graphene, Cambridge, pp. 81−85.

74. Toh, S.Y., Loh, K.S., Kamarudin, S.K., Daud, W.R.W., 2014, "Graphene production via electrochemical reduction of graphene oxide: Synthesis and Characterization." Chem. Eng. J., Vol. 251, pp. 422−426.

75. Chakrabarti, M.H., Low, C.T.J., Brandon, N.P., Yufit, V., Hashim, M.A., Irfan, M.F., Akhtar, J., Ruiz−Trejo, E. and Hussain, M.A., 2013, "Progress in the electrochemical modification of graphene−basedmaterials and their applications." Electrochim. Acta, Vol. 107, pp. 425−430.

76. Dogan, H.O., Ekinci, D. and Demir, U., 2013, "Atomic scale imaging and spectroscopic characterization of electrochemically reduced graphene oxide." Surf. Sci., Vol. 611, pp. 54−61.

77. Zhou, M., Wang, Y., Zhai, Y., Zhai, J., Ren, W., Wang, F. and Dong S., 2009, "Controlled synthesis of large−area and patterned electrochemically reduced graphene oxide films." Chem. Eur. J., Vol. 15, pp. 6116−6122.

78. Kakaei, K., 2015, "Decoration of graphene oxide with Platinum Tin nanoparticles for ethanol oxidation." Electrochim. Acta, Vol.165, pp. 330−335.

79. Kakaei, K. and Balavandi, A. 2017, "Hierarchically porous fluorine−doped graphene nanosheets as efficient metal−free electrocatalyst for oxygen reduction in gas diffusion electrode." J. Colloid. Interf., Sci. Vol. 490, pp. 819–824.

80. Kakaei, K. and Zhiani, M., 2013, "A new method for manufacturing graphene and electrochemical characteristic of graphene−supported Pt nanoparticles in methanol oxidation." J. Power Sources, Vol. 225, pp. 356−359.

81. Kakaei, K., 2013, "One−pot electrochemical synthesis of graphene by the exfoliation of graphite powder in sodium dodecyl sulfate and its decoration with platinum nanoparticles for methanol oxidation." Carbon, Vol. 51 pp. 195−202.

82. Kakaei, K. and Gharibi, H., 2014, "Palladium nanoparticle catalysts synthesis on graphene in sodium dodecyl sulfate for oxygen reduction reaction." Energy, Vol. 65 pp.166−202.

83. Yang, Y., Lu, F., Zhou, Z., Song, W., Chen, Q. and Ji, X., 2013, "Electrochemically cathodic exfoliation of graphene sheets in room temperature ionic liquids N−butyl, methylpyrrolidiniumbis(trifluoromethylsulfonyl)imide and their electrochemical properties." Electrochim. Acta, Vol.113, pp. 9−16.

84. Gürsu, H., Gençten, M., and Şahin, Y., 2017, "One−step electrochemical preparation of graphene−coated pencil graphite electrodes by cyclic voltammetry and their application in vanadium redox batteries." Electrochimica Acta, Vol. 243, pp. 239–249.

85. Goldstein, J., Newbury, D. E., Joy, D. C., Lyman, C. E., Echlin, P., Lifshin, E., Sawyer, L. and Micheal, J. R., 2003, "Scanning Electron Microscopy and X-ray Microanalysis." Springer, Chap 9, pp. 21−60.

86. Stokes, D. J., 2008, "Principles and Practice of Variable Pressure/Environment al Scanning Electron Microscopy (VP-ESEM)" Chap 2, pp. 17-62, John Wiley & Sons.

87. Linden, D. and Reddy, T.B., 2002, "Handbook of batteries" Chap 1, Sec. 1.3.1, McGraw−Hill, 3rd. Ed.

88. Bockris, J. O'M. and Reddy, A. K. N., 1970, "Modern Electrochemistry." Plenum, New York, Vol. 2, pp. 644−650.

89. Broadhead, J. and Hills, G. J., 1967, J. Electroanal. Chem., Vol. 13, pp. 354−355.

90. Warburg, E., 1899, Ann. Phys., Vol. 67, pp. 493−494.

91. Randles, J. E. B., 1947, Disc. Faraday Soc., Vol. 1, pp.11−13.

92. Rozental, K., and Ershler, B. V., 1948, Zh. Fiz. Khim,.Vol. 22, pp.1344−1346.

93. Sathyanarayana, S. Venugopalan, S. and Gopikanth, M. L., 1979, J. Appl. Electrochem., Vol. 9, pp.129−133.

94. Karunathlaka, S. A. G. R., Hampson, N. A., Leek, R. and Sinclair, T. J., 1980, J. Appl. Electrochem., Vol. 10, pp. 357−360.

95. Wang, C., 1998, "Kinetic Behavior of Metal Hydride Electrode by Means of AC Impedance." J. Electrochem. Soc., Vol. 145 pp. 1801−1805.

96. Sun, H., Wang, W., Yu, Z., Yuan, Y., Wang, S. and Jiao, S., 2015, "A new aluminium−ion battery with high voltage, high safety and low cost." Chem. Commun., Vol. 51, pp. 11892−118995.

97. Jiao, H., Wang, C., Tu, J., Tian, D. and Jiao, S., 2017, "A rechargeable Al−ion battery: Al/molten $AlCl_3$–urea/graphite." Chem. Commun., Vol. 53, pp. 2331−2334.

98. Kravchyk, K. V., Wang, S., Piveteau, L. and Kovalenko, M. V. Chem. Mater. 2017, "Efficient Aluminum Chloride−Natural Graphite Battery." Vol. 29, pp. 4484−4492.

99. Angella, M., Pana, C.J., Ronga, Y., Yuana, C., Lin M.C., Hwang, B.J. and Daia, H., 2017, "High Coulombic efficiency aluminum−ion battery using an $AlCl_3$−urea ionic liquid analog electrolyte." PNAS, Vol. 114, pp. 834–839.

100. Wang, D. Y., Chuan, Y. W., Lin, M. C., Pan, C. J., Chou, H. L., Chen, H. A., Gong, M., Wu, Y. P., Yuan, C., Angell, M., Hsieh, Y. J., Chen, Y. H., Wen, C. Y., Chen, C. W., Hwang, B. J., Chen, C. C., and Daet, H., 2017, "Advanced rechargeable aluminium ion battery with a high−quality natural graphite cathode." Nat. Commun., Vol. 8, pp. 14283−14289.

101. Gelman, D., Shvartsev, B. and Ein−Eli, Y., 2014, "Aluminum–air battery based on an ionic liquid Electrolyte." J. Mater. Chem. A, 2, pp. 20237−20242.

102. Zhang, L., Zhang, C., Ding, Y., Meyers, K.R. and Yu, G., 2017, "A Low−Cost and High−Energy Hybrid Iron−Aluminum Liquid Battery Achieved by Deep Eutectic Solvents." Elsevier Inc. Joule, Vol. 1, pp. 623–633.

103. Tian, H., Zhang, S., Meng, Z., He, W. and Han, W.Q., 2017, "Rechargeable Aluminum/Iodine Battery Redox Chemistry in Ionic Liquid Electrolyte." ACS Energy Lett., Vol. 2, pp. 1170−1176.

104. Wu, Y., Gong, M., Lin, M.C., Yuan, C., Angell, M., Huang, L., Wang, D.Y. Zhang, X., Yang, Jiang., Hwang, B. J., and Dai, H., 2016, "3D Graphitic Foams Derived from Chloroaluminate Anion Intercalation for Ultrafast Aluminum−Ion Battery." Adv. Mater., DOI: 10.1002/adma.201602958.

105. Zhang, X., Tang, Y., Zhang, Fan. and Lee, C.S., 2016, "A Novel Aluminum–Graphite Dual−Ion Battery." Adv. Energy Mater., Vol. 6, pp. 1502588−1502594.

106. Wang, C., Li, J., Jiao, H., Tu, J., and Jiao, S., 2017, "The electrochemical behavior of an aluminum alloy anode for rechargeable Al−ion batteries using an $AlCl_3$–urea liquid electrolyte." RSC Adv., Vol. 7, pp. 32288–32293.

107. Jung, S.C., Kang,Y.J., Yoo, D.J., Choi, J.W. and Han, Y. K., 2016, " Flexible Few−Layered Graphene for the Ultrafast Rechargeable Aluminum−Ion Battery." J. Phys. Chem. C, Vol. 120, pp. 13384−13389.

108. Atkins, P. and Paula, J. D., 1997, "Physical Chemistry", Data Section, pp. 1005-1017, W. H. Freeman and Company, New York, 8th edition.

109. Choo, H., Kinumoto, T., Jeong, S., Iriyam, Y., Abe, T. and Ogumi, Z., 2007, "Mechanism for electrochemical oxidation of highly oriented pyrolytic graphite in sulfuric acid solution." J. Electrochem. Soc., Vol. 254 B pp. 1017−1022.

110. Acik, M., Lee, G., Mattevi, C., Pirkle, A., Wallace, R.M., Chhowalla, M., Cho, K. and Chabal, Y., 2011, "The role of oxygen during thermal reduction of graphene oxide studied by infrared absorption spectroscopy." J. Phys. Chem. C., Vol. 115 pp. 19761−19768.

111. He, H., Klinowski, J., Forster, M. and Lerf, A. 1998, "A new structural model for graphite oxide". Chemical Physics Letters. Vol. 287, pp. 53−56.

112. Hwang, H., Kim, H. and Cho, J., 2011, "MoS_2 Nanoplates Consisting of Disordered Graphene−Like Layers for High Rate Lithium Battery Anode Materials." Nano Lett., Vol. 11, pp. 4826−4830.

113. Su, D. and Wang, G., 2013, "Single−Crystalline Bilayered V_2O_5 Nanobelts for High−Capacity Sodium−Ion Batteries. ACS Nano, Vol. 7, pp. 11218− 11226.

114. Liang, Y., Feng, R., Yang, S., Ma, H., Liang, J. and Chen, J., 2011, "Rechargeable Mg Batteries with Graphene−Like MoS2 Cathode and Ultrasmall Mg Nanoparticle Anode." Adv. Mater., Vol. 23, pp. 640−643.

115. Zhao, X., Zhao−Karger, Z., Wang, D. and Fichtner, M., 2013, "Metal Oxychlorides as Cathode Materials for Chloride Ion Batteries." Angew. Chem. Int. Ed., Vol. 52, pp. 13621−13624.

116. Sun, B., Huang, X., Chen, S., Munroe, P. and Wang, G., 2014, "Porous Graphene Nanoarchitectures: An Efficient Catalyst for Low Charge−Overpotential, Long Life, and High Capacity Lithium−Oxygen Batteries." Nano Lett., Vol. 14, pp. 3145−3152.

117. Xie, X., Ao, Z., Su, D., Zhang, J. and Wang, G., 2015, "MoS2/Graphene Composite Anodes with Enhanced Performance for Sodium−Ion Batteries: The Role of the Two−Dimensional Heterointerface." Adv. Funct. Mater., Vol. 25, pp. 1393−1403.

118. Dahn, J. R. and Seel, J. A., 2000, "Energy and Capacity Projections for Practical Dual−Graphite Cells." J. Electrochem. Soc., Vol. 147, pp. 899−901.